NASA/CR-2001-210855

# Feasibility Study of Radiometry for Airborne Detection of Aviation Hazards

*Gary G. Gimmestad, Chris D. Papanicolopoulos, Mark A. Richards, Donald L. Sherman, and Leanne L. West*
*Georgia Tech Research Institute, Atlanta, Georgia*

June 2001

The NASA STI Program Office ... in Profile

Since its founding, NASA has been dedicated to the advancement of aeronautics and space science. The NASA Scientific and Technical Information (STI) Program Office plays a key part in helping NASA maintain this important role.

The NASA STI Program Office is operated by Langley Research Center, the lead center for NASA's scientific and technical information. The NASA STI Program Office provides access to the NASA STI Database, the largest collection of aeronautical and space science STI in the world. The Program Office is also NASA's institutional mechanism for disseminating the results of its research and development activities. These results are published by NASA in the NASA STI Report Series, which includes the following report types:

- TECHNICAL PUBLICATION. Reports of completed research or a major significant phase of research that present the results of NASA programs and include extensive data or theoretical analysis. Includes compilations of significant scientific and technical data and information deemed to be of continuing reference value. NASA counterpart of peer-reviewed formal professional papers, but having less stringent limitations on manuscript length and extent of graphic presentations.

- TECHNICAL MEMORANDUM. Scientific and technical findings that are preliminary or of specialized interest, e.g., quick release reports, working papers, and bibliographies that contain minimal annotation. Does not contain extensive analysis.

- CONTRACTOR REPORT. Scientific and technical findings by NASA-sponsored contractors and grantees.

- CONFERENCE PUBLICATION. Collected papers from scientific and technical conferences, symposia, seminars, or other meetings sponsored or co-sponsored by NASA.

- SPECIAL PUBLICATION. Scientific, technical, or historical information from NASA programs, projects, and missions, often concerned with subjects having substantial public interest.

- TECHNICAL TRANSLATION. English-language translations of foreign scientific and technical material pertinent to NASA's mission.

Specialized services that complement the STI Program Office's diverse offerings include creating custom thesauri, building customized databases, organizing and publishing research results ... even providing videos.

For more information about the NASA STI Program Office, see the following:

- Access the NASA STI Program Home Page at ***http://www.sti.nasa.gov***

- E-mail your question via the Internet to help@sti.nasa.gov

- Fax your question to the NASA STI Help Desk at (301) 621-0134

- Phone the NASA STI Help Desk at (301) 621-0390

- Write to:
  NASA STI Help Desk
  NASA Center for AeroSpace Information
  7121 Standard Drive
  Hanover, MD 21076-1320

NASA/CR-2001-210855

# Feasibility Study of Radiometry for Airborne Detection of Aviation Hazards

*Gary G. Gimmestad, Chris D. Papanicolopoulos, Mark A. Richards, Donald L. Sherman, and Leanne L. West*
*Georgia Tech Research Institute, Atlanta, Georgia*

National Aeronautics and
Space Administration

Langley Research Center
Hampton, Virginia 23681-2199

Prepared for Langley Research Center
under Contract NAS1-99073

June 2001

Available from:

NASA Center for AeroSpace Information (CASI)
7121 Standard Drive
Hanover, MD 21076-1320
(301) 621-0390

National Technical Information Service (NTIS)
5285 Port Royal Road
Springfield, VA 22161-2171
(703) 605-6000

# Contents



# Tables

# Figures



# Appendices

## Executive Summary

This report describes the results of investigations by the Georgia Tech Research Institute (GTRI) into the feasibility of developing radiometric sensors for airborne detection of aviation hazards. In the first phase of the project, GTRI surveyed a wide range of proposed radiometric detection techniques. After this survey, three candidate techniques were selected for further study: millimeter-wave (MMW) sensing of icing conditions; infrared (IR) sensing of turbulence; and IR sensing of ash and acid clouds caused by volcanic eruptions.

None of these techniques is currently employed in a commercial sensor, yet the physical principles of each one are clearly documented, and all have been investigated in some detail. These features make the techniques good candidates for further research, with the possibility of developing and flight testing prototype sensors in the near term.

The radiometric sensing techniques described in this report are in various stages of development. Dual-polarization microwave radiometry emerged as the only viable radiometric technique for detection of icing conditions, but this technique is the least advanced in the sense that such a sensor has never been flight tested in association with icing. However, this method has been actively investigated during the past two years by means of simulations, and supporting data were acquired with a polarimetric radiometer in icing conditions on a mountaintop. The radiometer technology is mature and available, and GTRI recommends that more research, particularly flight tests, be conducted to assess the usefulness of dual-polarization MMW radiometry to the aviation community. Further simulation and modeling work is also required. Some of this research is currently under way as a Phase II SBIR effort by Radiometrics, Inc.

IR radiometric techniques for sensing turbulence have a history that spans more than two decades. Honeywell has developed a prototype radiometric sensor and is currently investigating IR techniques with both simulations and flight tests, as an internal R&D effort. Radiometers cannot detect turbulence directly, but may be able to detect atmospheric temperature structures that are associated with turbulent regions of airspace. Many experimental and theoretical studies have been performed to examine the correlation between turbulence and the atmospheric temperature structure, and the radiometric techniques have been flight tested to some extent, but significant research questions remain.

GTRI recommends that better flight tests be conducted to acquire data that can be used to determine warning time, probability of detection, false alarm rate, and correlation of the sensor output with the severity of turbulence. These tests must include measurements of truth data, including both the temperature structure and the severity of the turbulence. One potential way of acquiring such data sets is to fly an IR sensor in conjunction with the National Oceanic and Atmospheric Administration SCATCAT (Severe Clear Air Turbulence Collides with Air Traffic) tests.

Detection of volcanic ash by passive IR imaging has its history in satellite remote sensing, using AVHRR data. The two-band image analysis technique has been adapted for airborne sensing by the Commonwealth Scientific and Industrial Research Organisation (CSIRO) in Australia with the goal of developing a commercial sensor. Although the technology base for this technique is mature, flight testing to date has been limited, and some developmental work remains to be completed. As suggested by CSIRO, an attractive feature of an IR volcanic ash sensor is its similarity to an IR turbulence sensor. This similarity potentially allows for the development of one radiometric sensor that would warn aircrews of both ash and turbulence. Such a dual-purpose sensor would be more acceptable and affordable to the commercial aviation industry than two separate sensors.

The sensors for all of the proposed IR hazard detection techniques are forward-looking, staring radiometers, imaging and non-imaging. Each sensor can be specified in terms of its angular, spectral, and temporal resolution, along with its field of view. The commonality in the technology suggests that one carefully-specified multi-spectral IR imager could be used in flight tests to evaluate and optimize all of the proposed techniques. GTRI investigated the availability of suitable commercial IR imagers, and located only one that covered the required spectral region, a hyperspectral imager manufactured by Surface Optics. The ability of this imager to emulate the sensors proposed by Honeywell and CSIRO (as well as other proposed IR imaging sensors) was then investigated in detail.

The Surface Optics imager, with the correct options and some special features, is shown to be capable of emulating the other proposed sensors. In addition, the imager features a FLIR (Forward-Looking Infrared) emulation mode, so it can also be used as a long-wave imaging system that produces video data. As such, the imager can be used by NASA for other research purposes, such as evaluating techniques for providing synthetic vision. GTRI recommends that NASA acquire this sensor and use it to evaluate and advance all of the proposed IR radiometric hazard detection techniques.

Finally, the inadequacy of the modeling and simulation support for much of the sensor development has become apparent. Nowhere is this limitation more obvious than in turbulence detection. There is currently only one data set that includes both temperatures and wind fields with sufficient spatial resolution for simulating Honeywell's approach. This data set is a model of the Evergreen incident that was developed by the National Center for Atmospheric Research (NCAR). The Evergreen incident was an extreme event: a cargo aircraft lost an 18-foot section of one wing (including an engine) during an encounter with turbulence caused by a collision of the jet stream with a mountain wave. Clearly, other data sets are needed, spanning a range of turbulence severity. This problem is just one example of the inadequacy in modeling and simulation support.

GTRI recommends that a much more extensive modeling and simulation capability be developed, and that the data from future flight tests of radiometric hazard detection techniques be analyzed and understood in the framework of simulation models. Because it is simply not feasible to fly a prototype sensor in all possible conditions, simulation is the only way that crucial questions in regard to probability of detection and false alarm rate can be assessed before a sensor system is actually deployed. Development of such a capability will be an extremely helpful step in getting a radiometric hazard sensor developed and deployed on commercial aircraft.

# 1 Introduction

This report describes the results of investigations performed by the Georgia Tech Research Institute (GTRI) under a task entitled "Feasibility Study of Radiometry for Airborne Detection of Aviation Hazards" funded by the Sensors Research Branch of the Airborne Systems Competency at NASA Langley Research Center. The investigations occurred in three subtasks. Subtask 1 identified the candidate aviation hazards and detection techniques. Subtask 2 addressed the current state-of-the-art for the chosen detection techniques, and Subtask 3 analyzed the cost of a prototype sensor to be used as a research sensor for investigation of sensor performance and suitability for proposed applications, as well as the cost and requirements for a commercial unit.

For the ten year period beginning in 1989, there have been a total of 19,475 aviation accidents, of which 4,422, or 22.7%, were weather related according to the data posted by the Federal Aviation Administration (FAA) Office of System Safety. This data, taken from reference [1] is given below in Table 1. While the number of aviation accidents has decreased in the last few years (1996, 1997, 1998), the percentage of weather-related accidents has remained roughly constant.

To understand the accident statistics more completely, a definition of an accident must be provided. The data given in Table 1 through Table 5 only include accidents involving United States aircraft. Also, the definition of an accident is very broad. Accidents range from a flight attendant receiving a broken ankle due to turbulence, to the catastrophic loss of an aircraft and hundreds of lives. [2]

Table 1. Percentage of Weather Related Accidents to Total Number of Accidents from 1989-1998

| Year | Total Accidents | Weather Accidents | Percentage of Weather Related Accidents to Total Accidents |
|---|---|---|---|
| 1989 | 2,383 | 679 | 28.5% |
| 1990 | 2,343 | 538 | 23.0% |
| 1991 | 2,290 | 467 | 20.4% |
| 1992 | 2,180 | 500 | 22.9% |
| 1993 | 2,136 | 447 | 20.9% |
| 1994 | 2,076 | 388 | 18.7% |
| 1995 | 2,135 | 463 | 21.7% |
| 1996 | 2,017 | 490 | 24.3% |
| 1997 | 1,591 | 366 | 23.0% |
| 1998 | 324 | 84 | 25.9% |
| | 19,475 | 4,422 | 22.7% |

Breakdowns of the specific weather-related causes for the aviation accidents from 1989 to 1998 by FAA category are given in Table 2 through Table 5. [3] FAA Category Part 91 represents the public use operators and/or light, privately owned aircraft; Part 135 represents the small charter airlines and/or commercial commuters; Part 137 represents the agricultural operators, and Part 121 represents the large commercial airlines. [4][5]

While commercial airlines have the fewest number of total accidents, turbulence plays the largest role at almost 85% of weather-related accidents. Overall for these 4 categories of aircraft, turbulence was involved in almost 14% of the accidents, and icing played a role in 11.5% of the accidents. Note that a single accident may have several causal factors. [3] Also note that volcanic ash is not listed in the FAA causes for weather-related accidents.

Table 2. Private Aircraft Weather-Related Accident Causes

| Part 91 Weather Related Accidents | | |
|---|---|---|
| Weather Cause | Total | Percentage of Grand Total |
| Winds | 2248 | 43.3 |
| Visibility/Ceiling | 1233 | 23.7 |
| Turbulence | 443 | 8.5 |
| Icing | 411 | 7.9 |
| Precipitation | 355 | 6.8 |
| Density Altitude | 326 | 6.3 |
| Thunderstorm | 116 | 2.2 |
| Windshear | 63 | 1.2 |
| Grand Total | 5195 | |
| Total Accidents | 3482 | |

Table 3. Agricultural Aircraft Weather-Related Accident Causes

| Part 137 Weather Related Accidents | | |
|---|---|---|
| Group Meaning | Total | Percentage |
| Winds | 84 | 52.5 |
| Density Altitude | 30 | 18.8 |
| Turbulence | 20 | 12.5 |
| Visibility/Ceiling | 10 | 6.3 |
| Icing | 9 | 5.6 |
| Windshear | 4 | 2.5 |
| Thunderstorm | 3 | 1.9 |
| Precipitation | 0 | 0.0 |
| Grand Total | 160 | |
| Total Accidents | 128 | |

Table 4. Charter/Commuter Aircraft Weather-Related Accident Causes

| Part 135 Weather Related Accidents | | |
|---|---|---|
| Group Meaning | Total | Percentage |
| Visibility/Ceiling | 152 | 36.5 |
| Winds | 99 | 23.8 |
| Precipitation | 78 | 18.8 |
| Turbulence | 30 | 7.2 |
| Icing | 28 | 6.7 |
| Density Altitude | 15 | 3.6 |
| Thunderstorms | 10 | 2.4 |
| Windshear | 4 | 1.0 |
| Grand Total | 416 | |
| Total Accidents | 247 | |

Table 5. Commercial Airlines Weather-Related Accident Causes

| Part 121 Weather Related Accidents | | |
|---|---|---|
| Group Meaning | Total | Percentage |
| Turbulence | 50 | 79.4 |
| Precipitation | 4 | 6.3 |

| | | |
|---|---|---|
| Icing | 2 | 3.2 |
| Thunderstorm | 2 | 3.2 |
| Winds | 2 | 3.2 |
| Density Altitude | 1 | 1.6 |
| Visibility/Ceiling | 1 | 1.6 |
| Windshear | 1 | 1.6 |
| Grand Total | 63 | |
| Total Accidents | 59 | |

Even though the FAA does not list volcanic ash as a weather-related cause of accidents for aircraft, it presents a serious hazard. During the past 15 years, 80 commercial jets have suffered serious damage due to ash, with 7 having experienced a loss of power during flight. In 1989, one such incident occurred in Anchorage, Alaska and inspired the first International Symposium on Volcanic Ash and Aviation Safety in July 1991. [6] As Gari Marberry writes, "The [1989] incident at Redoubt volcano is one of the most famous and dramatic accounts of an airplane entering an ash cloud." [7]

The day after the December 14th eruption of Redoubt volcano, a 747-400 commercial airliner suffered flame-out in all four engines after entering the ash cloud. Only after dropping 8,000 feet were the pilots able to re-start two engines. After several more attempts, the remaining two engines were re-started as well. Fortunately, the plane was able to land safely, but only after a great scare and 80 million dollars worth of damage. A more complete description of the incident, taken directly from reference [7], is given in Appendix A.

The likelihood of other such incidents occurring increases every year. Fifteen (±8) volcanoes a year distribute ash into aircraft flight levels. [6] With the Asia Pacific region being the fastest growing area for aviation, [8] the volcanoes located in the "Ring of Fire" (shown in Figure 1 [9]) that surrounds the Pacific Ocean pose the biggest threat for future air traffic.

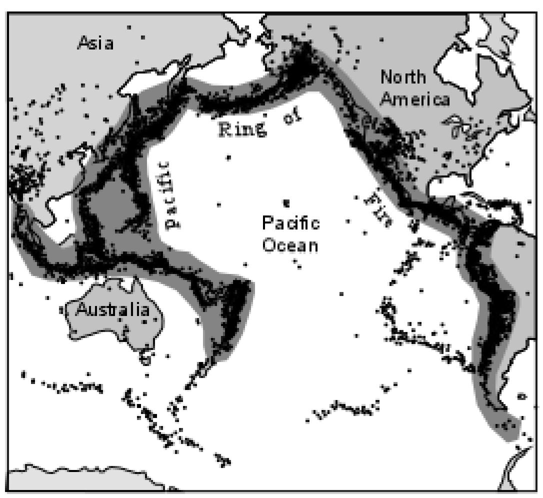


Figure 1. Ring of Fire Surrounds the Pacific Ocean

Listed below is a summary of forecasted statistics by a Swiss company, Air Transport Action Group (ATAG), in a 1997 report "Asia/Pacific Air Traffic Growth and Constraints". All forecasted statistics are for the year 2010. [8]

- The rate of growth in the Asia/Pacific region is twice that forecasted for the rest of the world, at an average of 7.4% per year through 2010.

- 1.1 billion passengers will be traveling to/from and within the Asia/Pacific region. This number is approximately equivalent to the 1995 total worldwide passenger traffic.
- The Asia/Pacific share of the worldwide passenger traffic (domestic & international combined) will grow to 42.9%.
- Traffic between North America (excluding Hawaii) and Northeast Asia will account for almost 73% of total transpacific passengers.
- The United States currently dominates the transpacific market, with a continuing domination of the predicted share by 2010, at 84%.

With close to half of the worldwide passenger traffic located in the Asia/Pacific region near the Ring of Fire and the United States controlling 84% of the transpacific market, a volcanic ash disaster involving an American commercial airliner is almost inevitable.

In the research project reported here, GTRI investigated the use of radiometry in airborne detection systems for weather-related aviation hazards. Radiometric sensors for aviation hazards are attractive, because they have the potential for widespread and inexpensive deployment on aircraft, using low-cost Monolithic Microwave Integrated Circuit (MMIC) or CCD infrared (IR) technologies. Radiometers could be deployed either as stand-alone sensors or as parts of sensor suites. Successful development of airborne radiometers to detect aviation hazards could enhance aviation safety while also providing benefits in efficiency of operations. However, further investigation of airborne radiometric hazard detection approaches will be required in order to develop reliable detection/discrimination techniques.

After a wide-ranging initial survey, GTRI adopted two criteria that a proposed technique must satisfy in order to be a viable candidate for further research: (1) a clear description of the physical principles of the hazard detection must be available; and (2) the proposed detection technique must have been investigated in some detail by others. These criteria were adopted to ensure that the science and technology of the proposed detection techniques were mature enough to allow one or more of the proposed techniques to be investigated in flight tests within the next few years. Table 6 shows the three candidate detection techniques that met both criteria.

Table 6. Candidate Hazard Detection Techniques

| | Icing | Turbulence & Wind Shear | Volcanic Ash |
|---|---|---|---|
| Infrared | | X | X |
| Microwave | X | | |

This report contains discussions of the three aviation hazards of interest - icing, turbulence, and volcanic ash, as well as candidate detection techniques for each hazard. Also included is a description of a hyperspectral imager by Surface Optics that meets the needs of simulating all of the various detection techniques for turbulence and volcanic ash.

The information presented in this report was gathered by a variety of means including, library resources, the internet, and personal contacts with the researchers who are developing the proposed new techniques as well as with others in the research communities. These contacts consisted of face-to-face meetings, e-mail notes, telephone conversations, and regular mail. A bibliography resulting from the literature search is given in Appendix F. During this process, GTRI has developed an extensive knowledge base on airborne radiometry applied to the three aviation hazards investigated.

# 2 Icing

The icing hazard occurs when droplets of super-cooled water come in contact with aircraft wing surfaces during flight. Small super-cooled droplets freeze quickly on the leading edges of the wings, where on-board de-icing equipment can eliminate their effect. [10] Larger size droplets, known as Super-cooled Large Drops (SLD), freeze more slowly. As a result, super-cooled water can run back over the airfoil where it freezes behind the de-icing boot, forming crusty ridges on the wing. Subsequently, aircraft performance can be seriously degraded due to a decrease in lift, while drag, weight, and stall speed can increase beyond safe limits. These conditions can bring down an airplane in minutes, and both military and general aviation accidents have been linked to them. [10] More information on the phenomenology of icing can be found in Appendix B.

Ideally, a detector for icing conditions would remotely sense the temperature, phase, and size of cloud particles (hydrometeors) ahead of an aircraft, as well as their range. This level of detail will not be available from a passive sensor, but development of a useful and practical technique may still be possible.

A minimum detection range of 5 km has been unofficially set by the comments of pilots, who consider this distance to be the minimum range that will allow them to activate de-icing equipment, ascertain proper functioning, and allow them to navigate around the hazard. [11] This range has been extended to 10 km by researchers.

## 2.1 Millimeter Wave Radiometry

The aircraft icing hazard occurs within clouds that are opaque at optical wavelengths. This condition necessitates the use of remote sensing techniques employing microwaves or millimeter waves (MMW). A primary challenge is to discriminate between the phases of water, that is, super-cooled liquid water (SLW) versus ice. This discrimination may be achievable by exploiting parameters such as frequency and polarization and by scanning the radiometer's pointing angle.

Clear air is a semi-transparent medium for millimeter waves. A radiometer aimed on a slant path to space measures a brightness temperature that is due only to emission and absorption by air molecules along the path. However, hydrometeors on the path cause an additional phenomenon: scattering. Scattering can bring radiation propagating in other directions into the radiometer’s field of view - for example, upwelling radiation from the warm earth. If ice crystals are involved, the scattered radiation may have a preferred polarization, because ice crystals are not symmetrical, and aerodynamic forces orient them as they fall. The orientation of ice crystals has previously been exploited with radar techniques that measure scattering differences between horizontal and vertical polarizations, thereby distinguishing the ice crystal phase from the liquid droplet phase. [12]

The polarimetric approach for discriminating between the phases of hydrometeors was investigated during the Mount Washington Icing Sensors Project (MWISP), which was conducted in April 1999 on Mount Washington in New Hampshire. Mount Washington frequently has cloudy and super-cooled conditions at the summit, and freezing drizzle occurred on several occasions during MWISP. During this experiment, personnel from the National Oceanic and Atmospheric Administration Environmental Technologies Laboratory (NOAA-ETL) investigated passive radiometry by using a unique instrument, the Polarimetric Scanning Radiometer (PSR). The PSR, developed by Dr. Albin Gasiewski, consists of a set of five polarimetric radiometers housed within a gimbal-mounted scanhead drum. The scanhead can aim the radiometers through a wide range of angles and also at external hot and ambient temperature calibration sources. The data recorded by NOAA-ETL at MWISP are the only data ever recorded to support the polarimetric icing sensor concept described above. Unfortunately, the data are still being analyzed, and the results are not yet available.

## 2.2 Current Status

The current work of the aviation icing hazard community, as it relates to the passive radiometric detection technique discussed here, is focused in three main areas:

a) Compilation of data bases from measurements and observations around the world to determine the frequency of mixed phase cloud encounters and to investigate cloud microphysics mechanisms influencing icing [13];

b) Analysis of comprehensive polarimetric measurements at MWISP [14]; and

c) Simulation of radiative transfer in mixed phase clouds at different altitudes and frequencies with models that include both emission and scattering. [15]

Research and development work on the design and development of radiometer systems suitable for icing detection is currently limited to the development in progress by Radiometrics Corporation. No other development activity has been identified during the course of our investigation.

## 2.3 Industry Activity

Radiometrics Corporation of Boulder, Colorado is in Phase II of an SBIR project under contract NAS3-00051. Andrew L. Reehorst of the NASA Glenn Research Center is the Contacting Officer's Technical Representative. Dr. Fredrick Solheim, president of Radiometrics and principal investigator on the project, furnished a copy of the Phase I final report to GTRI. [16] Some technical information from the report follows.

The proposed discrimination technique was based on a scanned dual-polarization radiometer that measures the brightness temperatures $T_v$ and $T_h$ for the vertical and horizontal polarizations. The first ($S_1$) and second ($S_2$) Stokes parameters are then found from the relations

$$S_1 = (T_v + T_h)/2 \text{ and}$$

$$S_2 = T_v - T_h .$$

Radiometrics Corporation investigated the potential for discrimination between liquid water and ice crystals using these Stokes parameters. The basic discrimination principal is that ice crystals fall with their long axes horizontal, so radiation scattered by them is preferentially polarized in the horizontal direction. Droplets are spherical and therefore they are isotropic scatterers. Sideways radiation scattering off of a sphere will have vertical polarization. In the MMW region at flight altitudes, side-welling and down-welling atmospheric radiation are very different, corresponding to brightness temperatures of perhaps 260 K sideways and 160 K down. The value of $S_2$ for droplets is therefore positive, and the radiometric signature of liquid water drops is a broad peak in $S_2$ as the radiometer is vertically scanned across the horizon. The signature of ice crystals has negative $S_2$ values at angles slightly above the horizon, switching abruptly to positive values below the horizon. The behavior of $S_2$ is caused by differences in the scattering properties of water droplets and ice crystals.

The first Stokes parameter, $S_1$, is several orders of magnitude greater for liquid water than for ice when viewing slightly above the horizon. This distinction is caused by differences in the emission from water droplets and ice crystals. Because the two effects have different physical mechanisms (scattering and emission), they yield independent measures of icing conditions, which helps to reduce ambiguities.

The approach taken by Radiometrics was to perform simulations using four different sets of measured microphysical cloud data. The simulations required a millimeter wave radiative transfer (MRT) model that included scattering. This model was not available, so Radiometrics developed their own model, based on an MRT code provided by Dr. Albin Gasiewski of NOAA-ETL.

Seven MMW frequencies were considered (60, 89, 118, 130, 160, 183, and 190 GHz). Simulations were carried out at several of these frequencies for three altitudes through a cloud with three SLD concentrations (a total of nine cases), scanning from zenith to nadir. Initial results indicated that the 89 GHz channel gave the best detection of liquid water, while also having the advantage of being in a 6-GHz wide quiet band where transmissions are not allowed. The discrimination signal was 5-10 K and Radiometrics expects to obtain 0.1 K resolution with their radiometer, therefore the signal-to-noise ratio would be as high as 20 dB. The simulations also showed that all of the useful data is in a scan angle range of +/-20 degrees about the horizontal.

However, later results (after careful checking and de-bugging of the MRT code) showed that the discrimination signal for ice would only reach about 0.4 K, even at the higher frequency of 130 GHz, and that the water signature essentially disappeared. For this reason, Radiometrics and the NASA Glenn Research Center are re-evaluating the airborne sensing approach. An alternative would be to equip airports prone to icing with ground-based sensors, probably including both radiometers and radars. The utility of airborne radiometric sensors for icing is considered an open question at this point.

As mentioned earlier, the only measured polarimetric data in icing conditions is from MWISP, and it has not yet been analyzed by NOAA-ETL. However, Radiometrics conducted an analysis of seven hours of the MWISP data, and found a strong subjective correlation of ice versus mixed phase with the radiometer data. They also found several limitations caused by ground-based data acquisition, and suggested that airborne experiments will yield much more definitive results. Confounding problems included the fact that the type of hydrometeor changed rapidly, (on a 5-minute time scale) so a homogeneous cloud was probably not present, and the wind direction was not necessarily along the radiometer’s aiming direction.

Radiometrics also updated a bibliography of aircraft icing publications furnished by Marcia Politovich of the National Center for Atmospheric Research (NCAR). This bibliography is included in their final report as a 25-page appendix.

Finally, although radar systems are beyond the scope of this investigation, it is perhaps worthwhile mentioning that strong support for a polarization measurement approach is given by a recent radar depolarization icing detection study by NOAA-ETL that was presented in a report to the FAA. [17]

## 2.4 Cost Estimates

### *2.4.1 Research Instrument*

The cost to acquire a one-channel radiometer operating at a single frequency band, with no on-board display, would be about $100,000. This estimate was furnished by Radiometrics, Inc. [15]

### *2.4.2 Commercial Sensors*

For a commercial system, the cost of components could be reduced through the use of Low Noise Amplifiers (LNA) and MMIC modules. These components can be produced at a substantially reduced cost, particularly in large numbers (that is, thousands of units). As a result, the cost of components per commercial unit is estimated to be in the range of $20,000 - $25,000. The final sales price per unit would probably be in the range of $50,000 - $75,000. This estimate was developed in a discussion with Radiometrics and NOAA personnel. [14][15]

### 2.5 Recommendations for Future Research

The highest priority research effort is the completion of the MWISP data analysis since these data resulted from the only dual-polarization radiometer measurements in icing conditions ever recorded, and other instruments at the MWISP field experiment have shown that Supercooled Large Drops (SLDs) were observed during this field experiment. During this analysis, the following is necessary:

a) Determine the degree of data correlation with ground observations such as those from the Cloud Particle Imager (CPI);

b) Determine the degree of data noise contribution from phenomena such as variations in the structure of the observed cloud during the scan;

c) Provide a data base for comparison with the radiative transfer codes that include a rigorous treatment of scattering, such as the code developed by NCAR;

Radiative transfer code validation and code-testing should proceed concurrently with the data analysis, and the codes should be used to simulate a variety of mixed phase scenarios.

Flight tests must be conducted to investigate whether structure changes within the observed cloud (gaps, breaks) can yield reduced values for the first Stokes parameter, which could be confused with the presence of SLDs. If the cloud structure does cause this problem, it will be necessary to measure the Integrated Path Water Content (IPWC), which can be used as a normalization factor. IPWC measurements, usually done via a differential attenuation method, require radiometric measurements at two different frequencies, for example at 89 and 35 GHz. As a result, the research radiometer design described above may need to be expanded so as to include a second channel to allow for IPWC measurements.

In the commercial instrument development area, it will eventually be necessary to resolve the issue of radome de-icing for a forward looking radiometer, due to the potential adverse impact of icing on radiometric resolution.

## 3 Clear Air Turbulence

Turbulence is defined as "random, unpredictable motion that occurs at the boundary between layers of air moving at different speeds." [18] When the layers of air moving at different speeds and directions come in contact with one another, the air space fragments into disturbances, or turbulence. [18]

Clear air turbulence (CAT) is the leading cause of non-fatal injuries aboard aircraft. [19] CAT, as its name implies, is not associated with stormy skies, but rather is encountered in cloudless skies. This section will discuss turbulence and some of the current techniques under investigation for remote sensing of this problem.

### 3.1 Turbulence Forecasting Research

Several organizations currently make forecasts of turbulent conditions, including the NOAA Forecast Systems Laboratory (NOAA-FSL) and the FAA's Aviation Weather Research Program (AWRP). [19][20] While aiding in the improvements of current forecasting models, the research conducted by these organizations may also prove useful in better understanding the structure of the atmosphere and the various parameters of air turbulence.

According to the NOAA public affairs website, [20] since 1998, NOAA-FSL has been conducting a research program named called Severe Clear Air Turbulence Collides with Air Traffic (SCATCAT). The purpose of SCATCAT is to improve forecast and warning services for aviation safety as related to clear air turbulence at altitudes above 20,000 feet. This improvement is being accomplished through an experimental program to document the environmental setting, generation, structure, and evolution of jet steam/frontal zone systems and associated turbulence, and by designing and verifying diagnostic and prognostic turbulence formulations for these phenomena in high-resolution numerical weather prediction models. [21]

During the SCATCAT missions, dropwindsondes are released in a “curtain” to acquire high spatial resolution measurements of temperature, pressure, and moisture. The curtains are as much as 400 km in length, with sondes being dropped as frequently as every 30 km. The vertical resolution of the measurements is as typically 15 m, and the absolute positions of the sondes are measured to cm accuracy with GPS receivers. [22]

Analysis of the data from SCATCAT flights in 1998 and 1999 showed small-scale layers, a few hundred meters in depth, that were conducive to CAT, but there were no flight observations to confirm that turbulence was actually present. These results identified the need for an independent measurement of turbulence. One way to confirm that turbulence occurs is to fly another aircraft through the region of the soundings. NOAA researchers have recently developed another approach, which is to derive the turbulent air motions from the position-versus-time data for the dropsondes. The GPS position data is sufficiently accurate to make this a technique viable. [21][22]

During the winter of 2000-2001, SCATCAT missions with the NOAA G-IV aircraft were flown over the southeastern US, offshore of the eastern seaboard, over the Gulf of Mexico, and over the northeastern Pacific Ocean. Flights were also conducted above and down-stream from deep cumulus convection.

SCATCAT researchers intend to propose another field program for the winter of 2001-2002. The location and details have not yet been determined, but the experimental procedure will require two aircraft, one for releasing dropsondes and the other for observing turbulence ahead of the sondes. Both aircraft will then fly vertical profiles through the air space of the soundings. [21]

The FAA's AWRP is also trying to garner more accurate data for the turbulence forecasting models. An on-board algorithm is being installed in the software of commercial aircraft to provide objective measurements of the severity of turbulence encountered. Currently, pilots give subjective opinions on the severity of the incident, and pilot reports, if given at all, could be ambiguous as to the time and location of the incident. [19] The AWRP automated system should provide a more complete assessment of turbulence encounters.

## 3.2 Methods of Detection

All radiometric techniques for turbulence detection rely on atmospheric temperature structures that depart from the standard adiabatic lapse rate of the non-turbulent atmosphere. The radiometric techniques are indirect in the sense that they do not measure turbulent motion. Rather, they measure the temperature structure of the atmosphere ahead of the aircraft and attempt to relate it to the likelihood that turbulence will be experienced.

Researchers have been studying passive IR detection of turbulence for decades. In the 1970's, Peter Kuhn developed an IR radiometer that was flown and tested on three NASA aircraft in the 1979 Clear Air Turbulence Flight Test Program. Kuhn's passive IR system detected CAT by detecting water vapor variability ahead of the aircraft. In non-CAT conditions, the water vapor content is constant. The detector had a false-alarm rate of less than 8% in clear air at altitudes above 4.4 km with a range of 60 km. However, the system was not tested with clouds in the vicinity. [23]

## 3.3 Kuhn and Sinclair 'S' Layer Model and FLIR Sensor System Design

In the early 1990's, Kuhn and Sinclair developed an 'S' layer model to describe the instabilities that lead to clear air turbulence and then derived the specifications of a forward looking infrared (FLIR) sensor system capable of detecting the clear air turbulence hazard. [24] Kuhn and Sinclair's specifications are given in Table 7.

Table 7. FLIR Sensor System Specifications

| | |
|---|---|
| Wavelength | 12.8 to 14.3 μm |
| Field of View | 10° |
| Bandwidth | 1.5 μm |
| Noise Equivalent Radiance | $0.169 \times 10^{-6}$ W/cm$^2$sr<br>at a scanning rate of 1 frame/second |
| Detector | HeCdTe with<br>Area = $1 \times 10^{-4}$ cm$^2$/pixel |
| Optics Area | 125 mm$^2$ |
| Optics Transmission | 0.32 |

The 'S' layer model was developed from flight tests conducted by the Air Force during the High Altitude Clear Air Turbulence (HICAT) program. It is important to note that during the analysis of the HICAT data, Kuhn and Sinclair claimed that large angle crossings of the horizontal temperature variations that comprise the 'S' Layers are necessary. Flight paths parallel to warm and cool troughs and ridges were said to yield insignificant temperature variations. [24]

See Appendix C for more information on Kuhn and Sinclair's 'S' layer model, as well as further information on clear air turbulence in general.

## 3.4 Industry Activity

As mentioned earlier, radiometric techniques sense the *conditions* that give rise to turbulence, as opposed to detecting *turbulent motion*. [25] Honeywell is currently pursuing CAT detection by passive IR radiometry. Their approach is to estimate the Richardson number, Ri, which is a measure of instability. Low Ri values are taken as an indication of turbulent conditions. They claim that turbulence will be encountered in 70 - 80 % of cases when Ri is less than 0.25 and in 100 % of cases when Ri is 0.15 or less. [26] Their goal is to estimate Ri in real time at sufficient range so that the pilot and the aircrew can take appropriate measures.

Honeywell researchers built their first radiometer to test this concept four years ago. Two years ago, they performed mountaintop measurements with a newer version. The purpose of these tests was to validate their wind shear algorithm, which is based on measurements of horizontal temperature gradients. The radiometer was pointed in four directions from a mountaintop and the resulting data were analyzed to predict the wind shear between 13,000 and 18,000 feet of elevation. Wind data from nearby balloon sondes was used as truth data. The researchers reported that the tests were successful. The radiometer is being modified for use in further ground tests that will be aimed at detection of turbulent conditions associated with mountain waves. [27]

### *3.4.1 Sensor Design*

The following summary is taken from a Honeywell power point presentation. [28] Honeywell's prototype sensor is a forward-looking IR radiometer operating in the $CO_2$ band. The sensor is scanned primarily in an azimuthal plane, but it can also be scanned vertically. Detection of turbulence by the sensor involves four steps:

1) Measuring radiance values
2) Correlating the radiance values to temperature and effective range
3) Determining the wind shear and vertical temperature profile from the temperature map using known meteorological algorithms
4) Calculating Ri

Honeywell has been actively investigating their proposed sensing technique for 4 years, by means of both radiative transfer calculations and field measurements. The commercial version of the sensor is envisioned as a cylinder twelve inches long and three inches in diameter, with a 2 - 3 inch IR window in one end. A diagram of the Honeywell sensing geometry is shown in Figure 2, and the sensor specifications are given in Table 8.

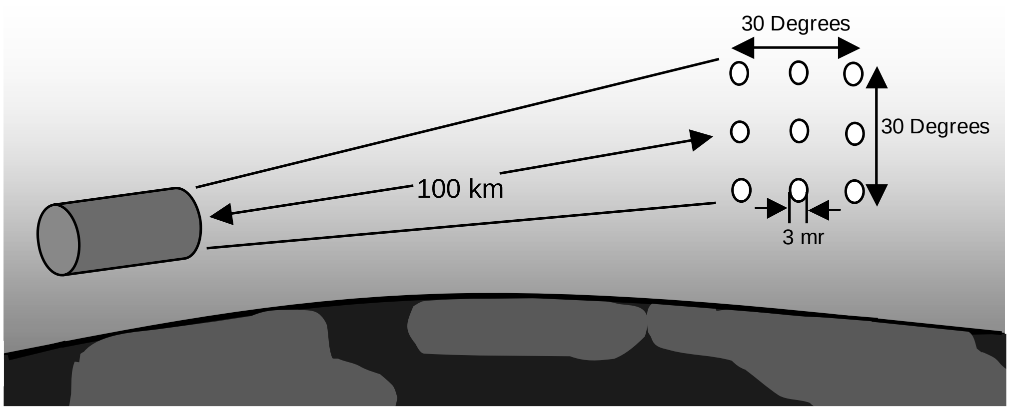


Figure 2. Honeywell Sensing Geometry Diagram

Table 8. Honeywell Sensor Specifications

| | |
|---|---|
| Wavelength | 12.2 μm |
| Overall Field of View | ±15° Vertical<br>±15° Horizontal |
| Bandwidth | Narrow |
| Effective Range | 100 km |
| Spatial Resolution | 300 m at 100 km |
| Temperature Resolution | < 0.1K with an integration time of 10 ms |

The Honeywell radiometer is not an imaging system. It obtains angular resolution through the use of multiple fields of view (FOVs). The FOVs are arranged in a 3 X 3 square array, aimed at angles in a range of ± 15 degrees horizontally and vertically, as shown in Figure 2. Each FOV is only 3 - 6 mrad wide.

A narrow-band optical filter is used to define a bandpass centered at 12.2 microns. This choice of wavelength results in an effective range of about 100 km at flight altitudes. Note that a 3 mrad FOV corresponds to a spatial resolution of 300 m at the effective range of 100 km. Honeywell states that this resolution is essential for the success of their approach. [27]

The detectors in the research instrument are cooled with liquid nitrogen, and Honeywell researchers suggested that a Joule-Thompson cooler could be used in a commercial version. [27] The instrument has a temperature resolution of less that 0.1 K with an integration time of 10 ms. The measured signals associated with the atmospheric conditions that give rise to turbulence are said to be much larger than 0.1 K, so the measurements have a high inherent signal-to-noise ratio.

### 3.4.2 Radiative Transfer Calculations

Radiative transfer calculations are being performed to support Honeywell's research in conjunction with researchers at the National Center for Atmospheric Research (NCAR) in Boulder, Colorado. NCAR has done a detailed analysis of the Evergreen incident, in which a cargo aircraft lost an engine and part of a wing due to an encounter with turbulent air in 1992.

A wind profiling lidar was operating in the vicinity at the time of the incident, and the NCAR researchers have been able to reconstruct the wind field that caused the aircraft damage. The wind field is understood to have been a convergence of a mountain wave with the jet stream. NCAR has produced modeled data, including temperature fields and wind fields, to represent the Evergreen incident, with 200 m resolution vertically and 1,000 m resolution horizontally.

Honeywell's radiative transfer calculations were performed using the US Air Force FASCODE model, with the NCAR temperature data as input. Honeywell's calculations simulated flights at approximately ten different altitudes, approaching the turbulent region from two different directions. The modeled radiometric signals showed a good correlation with the turbulence conditions. The interaction between Honeywell and NCAR is ongoing.

### 3.4.3 Recommendations for Further Research

To date, both the radiative transfer calculations and the measurements have given encouraging results. Calculations using other data sets should be performed in order to see how robust the warning algorithms are. In this connection, the SCATCAT data sets could be processed to provide suitable temperature fields and wind fields in turbulence caused by breaking waves. [22]

Ultimately, the usefulness of Honeywell's technique will have to be assessed through flight tests. These tests should include different types of turbulence and a range of flight altitudes, and the tests must be supported with truth data.

### 3.4.4 Research Instrument Cost Estimates

The cost to procure a research instrument similar to Honeywell's device would be no more than $200,000. This estimate is based on previous experience costing similar devices at GTRI.

### 3.4.5 Commercial Sensors

Honeywell personnel commented that the cost of a commercial sensor would be similar to the cost of a radar system. [27]

Based on previous experience at GTRI, the production cost of a commercial radiometer head could be as low as $10,000. This estimate is based on an assessment of the total cost of procuring and fabricating all of the components, plus the cost of assembly. This cost does not include the cockpit display or the system software.

The sensors would, of course, sell for some multiple of the production cost, depending on the quantity.

# 4 Volcanic Ash

Approximately 60 volcanoes worldwide are active during a typical year, [29] and in the North Pacific Region of the United States alone, volcanic ash is present an average of 4 days a year where most jet aircraft fly. Volcanic ash causes millions of dollars in damage to the aircraft that accidentally fly though these clouds, while also posing a grave danger to pilots and passengers. [30] Ash clouds, the various types of damage that occur to aircraft due to these clouds, and the current techniques of detecting these clouds are discussed in this section.

## 4.1 Characteristics of Ash Clouds

When volcanoes erupt, they eject molten rock and volcanic gasses to altitudes higher than 12 miles. [31] As the column of gas and particles reaches the tropopause, it starts to flatten out due to a temperature inversion. The larger particles fall back to earth quickly, but the finer ash particles can remain suspended for years due to their elongated, parachute-like shape. [32]

While suspended in the atmosphere, the ash clouds can travel great distances by means of jet streams and other wind currents. [32] Less than three days after the June 15, 1991 eruption of Mount Pinatubo, its ash cloud had traveled more than 5,000 miles. [30] After 22 days, this same ash cloud had circled the globe and had spread to cover a band from 10 degrees south latitude to 20 degrees north latitude. [33]

The concentrations and elemental composition of the ejected volcanic ash and gasses can vary a great deal from volcano to volcano. Usually, volcanic ash consists mostly of silicon, aluminum, magnesium, and iron with lesser amounts of potassium, sodium, and calcium. [34] The three most abundant gasses are water vapor, carbon dioxide, and sulfur dioxide, respectively. Other gasses usually released include hydrogen sulfide, hydrogen, carbon monoxide, hydrogen chloride, hydrogen fluoride, and helium. [35] Table 9 [35] gives examples of the volcanic gas composition of three different volcanoes located around the world. The numbers given are volume percent concentrations of the specified gas.

Table 9. Volcanic Gas Composition

| Volcano | Kilauea Summit (Hawaii, USA) | Erta' Ale (Ethiopia) | Momotombo (Nicaragua) |
|---|---|---|---|
| Water Vapor | 37.1 | 77.2 | 97.1 |
| Carbon Dioxide | 48.9 | 11.3 | 1.44 |
| Sulfur Dioxide | 11.8 | 8.34 | 0.50 |
| Hydrogen | 0.49 | 1.39 | 0.70 |
| Carbon Monoxide | 1.51 | 0.44 | 0.01 |
| Hydrogen Sulfide | 0.04 | 0.68 | 0.23 |
| Hydrogen Chloride | 0.08 | 0.42 | 2.89 |
| Hydrogen Fluoride | -- | -- | 0.26 |

## 4.2 Damage Mechanisms

Volcanic ash clouds cause several types of immediate and long-term damage to aircraft. The immediate damage is usually the abrasion of exterior surfaces and the accretion of ash in aircraft surface openings. Abrasion and scratching of the windshield can diminish visibility, and abrasion to moving engine parts, such as the compressor and turbine blades, will decrease the engine efficiency. [36] Abrasion can also occur to the landing light covers and the navigation lights. [33]

Through engine surface openings, ash can enter the interior of an aircraft and spread throughout the air filter system and cabin. The aircraft's electronic system may be damaged by this interior ash, causing failure of navigation instruments and power generators. [36] However, the most hazardous problem occurs when the silicate ash encounters the engines' hotter parts and melts.

The melted ash forms a glassy coating that blocks cooling passages and coats fuel nozzles, the combustors, and the turbines, thereby causing immediate power loss in the engines. This power loss can occur in less than one minute. [33][36][37]

Some effects of the ash cloud may not be apparent for months or years. This long-term damage to aircraft includes fading of polyurethane paint, crazing of acrylic windows, and accumulation of mineral deposits such as gypsum and anhydrite in engine turbines. Crazing of acrylic windows was observed for years after the 1982 El Chichon volcanic eruption, and after the Mount Pinatubo eruption, some Asian airlines found that the buildup of mineral deposits blocked cooling holes, thereby causing engines to overheat. [33] Volcanic gasses that have been converted to acids can also cause structural weakening over time by damaging rubber seals, lubricants, and plastics. [37]

## 4.3 Methods of Detection

Currently, pilots cannot distinguish a volcanic cloud from a meteorological cloud, either visually or with radar. [30] They must rely on satellite data and trajectory predictions to avoid the ash clouds of volcanoes. There are two satellite systems that can detect volcanic clouds. Once a day, the Total Ozone Mapping Spectrometer (TOMS) gathers volcanic cloud position data in the ultraviolet spectrum by detecting sulfur dioxide, one of the main gaseous components of volcanic clouds. [35][38] The other satellite system utilizes geostationary satellites with IR detectors. This satellite system is much more useful, because it can gather data every 15 to 60 minutes, as opposed to once a day. And while this system requires some data processing, it does not require the extensive data processing that the TOMS system requires. [33][38] This system also detects the ash cloud directly, using a two-band IR method. [38]

The two-band IR method of volcanic ash detection relies on the silicate particles of ash clouds having optical properties at certain wavelengths that are different from the water droplets of meteorological clouds. Therefore, using a multi-band IR method to calculate brightness temperature differences discriminates between volcanic clouds and meteorological clouds, and thus enables detection of the volcanic ash cloud. For further information on how the two-band IR system works, refer to Appendix D.

## 4.4 Industry Activity

The Commonwealth Scientific and Industrial Research Organisation (CSIRO) Division of Atmospheric Research located in Melbourne, Australia, has tested and patented the Airborne Hazards Detection System (AHDS), an airborne passive IR radiometer with a two-band detection technique similar to the AVHRR two-band system described in Appendix D. [39] Their work on the technique began with a study in 1986. In December 1990, CSIRO's first airborne tests of the model successfully detected the theoretically-calculated brightness temperature difference (BTD) of cumulus clouds at altitudes up to 8,000 meters.

In March 1991, ground-based tests in Japan near Mt. Sakurajima similarly detected the BTD of volcanic ash clouds. Following these trials, CSIRO obtained patents, including US Patent No. 5,602,543, *Detection System for Use in an Aircraft*. The researchers published several papers on both theoretical and experimental aspects of volcanic ash detection with their technique. [40][41][42][43] However, CSIRO states that further research is necessary to determine how the system will operate at commercial aircraft altitudes and what the optimum optical bandwidths are. The expected detection distance is 100 km to 200 km. [40]

CSIRO held discussions with the Boeing Aircraft Company beginning in 1990 in an effort to commercialize the sensor. Boeing suggested that a multi-function hazard warning system would receive far greater acceptance in the industry, so CSIRO has also investigated the detection of other hazards by passive IR radiometry. These other hazards include low-level clear air turbulence, sulphur dioxide ($SO_2$), and sulfuric acid ($H_2SO_4$). The multi-function system is known as the Airborne Hazard Detection System (AHDS).

The AHDS radiometer is planned as a 100X100 element detector array used in averaging mode to provide a two-dimensional 10X10 element display, with each element covering a solid angle of 1 degree by 1 degree. Warning time estimates are between 3 and 6 minutes. Instrument specifications for detection of the three hazards are given in Table 10 through Table 12, with composite system specifications, based on IR Focal Plane Array (FPA) technology, given in Table 13.

Table 10. Specifications for Volcanic Ash Detection

| | |
|---|---|
| Wavelengths | 10.5 and 11.9 μm |
| Bandwidth | 1.0 μm |
| Sensitivity | 0.2K at 270K |

Table 11. Specifications for $SO_2$ and $H_2SO_4$ Detection

| | |
|---|---|
| Wavelengths | 7.4, 8.6, 10.5, and 11.9 μm |
| Bandwidth | 1.0 μm |
| Sensitivity | 0.2K at 270K |

Table 12. Specifications for Clear Air Turbulence Detection

| | |
|---|---|
| Wavelength | 6.8 μm |
| Bandwidth | 0.5 μm |
| Sensitivity | 1.0K at 270K |

Table 13. Specifications for CSIRO's Multi-Function Thermal IR Radiometer

| | |
|---|---|
| Wavelength Range | 6.8, 7.4, 8.6, 10.5, and 11.9 μm |
| Optical System | Off-Axis Parabolic Reflector |
| Field of View | ±5° Vertical |
| | ±5° Horizontal |
| Entrance Aperture | 50 mm Diameter |
| Detector | 100X100 Element Pyroelectric Array |
| Bandwidth | 0.5 to 1.0 μm |
| Sensitivity | 0.2K at 270K |

CSIRO's research radiometer has a single FOV with a width of three degrees. It samples incident thermal radiation in one of five wavebands selected by interference filters. The temperature resolution is about 0.1 K with an integration time of 2 seconds. The radiometer is a stand-alone instrument, requiring only 12 VDC power. It uses a pyroelectric detector that requires no cooling, and it is self-calibrating. The radiometer assembly includes hot and cold calibration blackbodies.

For tests in Tasmania, the instrument was mounted in a pod under the wing of a Piper Navajo. The pod has also been mounted on the fuselage of an F27 for other measurements. The pod has a Germanium window. Unfortunately this window has poor transmittance for wavelengths below about seven microns, so CSIRO considers their clear air turbulence tests with this configuration to be incomplete. [44]

For tests in Japan, the radiometer was mounted in the cabin of a Cessna 404 using a 45-degree mirror to view in the forward direction while looking through an open port in a side window. The aiming direction of the radiometer during flight is recorded on videotape by using a video camera boresighted with the radiometer.

The radiometer has both analog and digital outputs. Data acquisition is accomplished with a laptop computer. All data acquisition hardware is mounted in a standard 19-inch rack.

In October 1999, CSIRO came to the United States and presented the AHDS to a number of airline and aerospace companies with the hopes of commercializing the technology. They were well received, but the process has not progressed due to internal changes within the companies visited. CSIRO is still interested in pursuing the commercialization of this sensor. [45]

## 4.5 Cost Estimates

### *4.5.1 Research Instrument*

The cost of the existing research instrument was about $100,000.

### *4.5.2 Commercial Sensor*

CSIRO estimates that a commercial instrument would cost between $50,000 and $100,000, depending on the demand and the exact configuration. They believe that it should be integrated into the cockpit instruments, with a three-stage warning system that would issue an audio alert, a visual alert (such as a flashing red light) and a 2-D color display of the view ahead. CSIRO suggests mounting the commercial sensor in the wing near the landing lights, or on the undercarriage.

Two other considerations affect the sensor cost: maintenance and training. Periodic maintenance will be required, so spare parts will have to be stocked, and a skilled staff must be trained to install and remove the sensors. Pilots will have to be trained in the use of the equipment, so a training video and manual must be supplied. These considerations will add to the full cost of implementing the sensor. [46]

## 4.6 Recommendations for Future Research

The detection techniques proposed by CSIRO must be demonstrated in an extensive series of flight tests, with complete supporting data, before they will gain wide acceptance. These tests would be primarily to validate the technique, but they could also be used to optimize the sensor in terms of the number and locations of the spectral bands; the required resolutions based on angle, temperature, and time; and the data processing algorithms. All of these parameters must be established before an accurate production cost can be calculated.

In addition, the volcanic ash research community has voiced a concern that must be addressed: although a volcanic ash sensor would be most valuable in the Pacific Rim where there are many volcanoes, this region of the global air space also tends to have many clouds. The sensor would sometimes fail to remotely detect an ash cloud because the sensor’s view would be blocked by a water cloud. [47] This concern should be addressed by a statistical analysis of the probability of a cloud-free line of sight between the aircraft and the ash cloud for various geographical locations around the globe.

# 5 Hyperspectral Imagers

Because turbulence, volcanic ash, and $SO_2$ and $H_2SO_4$ can all be detected using radiometers, the technique is well suited for a multi-function sensor. Combining the parameters for the aforementioned sensors gives the specifications for a radiometer that could emulate all of the proposed systems described above. Table 14 gives the combined specifications for such a radiometer.

Table 14. Specifications for a Multi-Function Thermal IR Radiometer

| | |
|---|---|
| Wavelength Range | 6.8 to 14.3 μm |
| Field of View | Up to ±15° Vertical |
| | Up to ±15° Horizontal |
| IFOV | ≤ 3 mr |
| Bandwidth | 0.1 to 1.5 μm |
| Temperature Resolution | 0.1 to 0.5 K |
| Pixel Format | 100 x 100 |
| Data Acquisition Rate | 1 to 100 Hz |

In subtask 2 [48], GTRI proposed that NASA should acquire an airborne forward-looking hyperspectral imager to support detection research for both the turbulence and the volcanic ash hazards. After an extensive search, GTRI has found only one commercially available unit that has the flexibility to cover most of the requirements of the multi-function radiometer described in the previous sections of this report.

This section and Appendix E describe the hyperspectral imaging instrument collection offered by Surface Optics Corporation in San Diego, CA. The Multi-band Identification and Discrimination Imaging Spectroradiometer (MIDIS) is configured as imaging heads, a processor, and data storage. One processor can accommodate up to three imaging heads. The Appendix is the MIDIS Performance Specifications document provided by the Vice President of Surface Optics, Mark Dombrowski. [49]

## 5.1 Principle of operation

The detectors in the imaging heads are 256 x 256 pixel focal plane arrays (FPAs). MIDIS does not, however, obtain hyperspectral data by imaging the whole scene onto an FPA at a set of different wavelengths. Rather, the imager observes a narrow slice of the scene, and its spectrum is spread across all rows of the FPA. A complete image is obtained by scanning the slice across the scene as in a push broom imager. This approach has the advantage that data at all wavelengths is being acquired at all times, which avoids spatial/spectral confusion in a time-varying scene.

Conceptually, a hyperspectral imager provides "cubes" of data, in which two axes of the cube correspond to the two-dimensional image data, and the third axis corresponds to the spectral information. Data rates are quoted in cubes per second rather than frames per second.

The dispersive element in MIDIS imaging heads is a prism. Prisms are used instead of gratings because they provide a wider spectral range (gratings only provide a factor of two in wavelength unless the order-sorting filters are changed).

The fact that the entire spectrum is spread across the rows of pixels in the FPA means that calibration must be done both spatially and spectrally. Calibration is accomplished initially with a laboratory blackbody and then periodically with an internal reference source. According to the vendor, it is possible to include the effects of additional optical elements, such as windows and mirrors, in the calibration. [50]

## 5.2 Spectral Coverage and Resolution

Three imaging heads are available: a visible near-IR head for 0.4 - 1.4 microns, a mid-wave IR head (MIDIS 2000M) for 2 - 5 microns, and a long-wave IR head (MIDIS 2000L) for 8 - 12 microns. Only the 2000L is of interest here.

The spectral resolution depends on how many spectral bands are recorded. There are two choices: 30 bands and 60 bands. For 30 bands, the spectral resolution at 10 microns is 0.14 microns and for 60 bands it is smaller by a factor of two, i.e. 0.07 microns. Note that the spectral resolution is not constant across the spectrum, but it varies by less than a factor of 1.8 across the 8 - 12 micron range.

The vendor states that the wavelength range can be extended. In fact, Surface Optics has already designed a 5 – 12 micron version of the 2000L. It would be more expensive due to the fact that it employs some aspheric elements. The upper wavelength limit can be extended to 14 microns by changing the specifications of the FPA. This extension would, however, have the effect of increasing the noise level in the image data.

## 5.3 Temperature Resolution

The temperature resolution of the MIDIS 2000L is not specified in the usual way as a temperature or radiance uncertainty. It is rather specified as a signal-to-noise ratio (SNR) when observing a 300 K grassy field at a distance of one kilometer (see the SNR Section of Appendix E).

In order to convert this ratio to a more familiar measure, GTRI has assumed that the SNR values would be roughly the same when viewing a 300 K blackbody, and that the SNR values correspond to the total radiance in a spectral band divided by the radiance uncertainty. Using the Planck radiation formula, GTRI found the radiance in a 1.0-micron band centered at each of three wavelengths, and then increased the temperature until the radiance had increased by the amount corresponding to the vendor's SNR specification. The resulting temperature differences are shown in Table 15 for the 30-band implementation at 300 K.

Table 15. MIDIS 2000L Temperature Resolution

| **$\lambda$ ($\mu$m)** | **$\Delta\lambda$ ($\mu$m)** | **$\Delta$T (K)** |
|---|---|---|
| 10.5 | 1.0 | 0.034 |
| 11.9 | 1.0 | 0.038 |
| 8.6 | 1.0 | 0.034 |

Comparing Table 15 to Table 14 shows that the reported MIDIS temperature resolution is about six times better than the requirements.

## 5.4 Temporal Resolution

The MIDIS system can be operated with either 30 or 60 spectral bands, and with image formats of 256 x 256, 128 x 256, or 128 x 128 pixels. Time resolution can be traded off against spatial and spectral resolution as shown in Table 16.

Table 16. Time Resolution vs. Spatial and Spectral Resolution

| Spatial Resolution | Spectral Resolution | Time Resolution |
|---|---|---|
| 256 x 256 | 30 Band | 3.75 cubes per second |
| 128 x 256 | 30 Band | 7.5 cubes per second |

| | | |
|---|---|---|
| 128 x 128 | 30 Band | 15 cubes per second |
| 256 x 256 | 60 Band | 1.875 cubes per second |
| 128 x 256 | 60 Band | 3.75 cubes per second |
| 128 x 128 | 60 Band | 7.5 cubes per second |

## 5.5 FLIR Emulation Mode

It should be noted that MIDIS is designed with an operating mode that emulates a FLIR, i.e. a broadband IR imager that provides video data at 30 frames per second. This mode would be useful in studies related to the Synthetic Vision program.

## 5.6 Data Storage

A hyperspectral imager has a high data rate, so a large data storage capacity is required for recording over any significant time period. Two RAID-based recording options are available for MIDIS. The data storage capacity and corresponding recording times are shown in Table 17. Note that larger recorders are available, and the product allows high-speed, real-time recording.

Table 17. Data Storage Capacity and Recording Times

| | **Option 1** | **Option 2** |
|---|---|---|
| **Storage Capacity** | 36 GB | 72 GB |
| **Recording Time** | 9 minutes | 18 minutes |

## 5.7 Field of View

The standard field of view (FOV) of the MIDIS imaging heads is $12° \times 12°$. However, custom fore-optics can be used to achieve other FOVs. In particular, an FOV of $30° \times 30°$ can be achieved. [50]

## 5.8 Emulation of Hazard Sensors

With a few exceptions, a properly specified Surface Optics LWIR MIDIS 2000L hyperspectral imager could be used to directly emulate the proposed sensors for turbulence, ash, $SO_2$ and $H_2SO_4$. The resulting hyperspectral data could then be used to optimize the design parameters and analysis algorithms of future operational sensors. Emulation of the proposed sensors is described in detail in the three sections below.

### *5.8.1 FLIRs*

The FLIR proposed by Kuhn and Sinclair (see Table 7) could be emulated by specifying an extended wavelength range for the MIDIS 2000L (to 14.3 microns). The standard MIDIS FOV is close to the proposed $10° \times 10°$ FOV. As shown in Table 16, the proposed frame rate of 1 Hz would be exceeded by any choice of spatial and spectral resolution.

The MIDIS system also has a FLIR emulation mode that uses the entire spectral range. As mentioned earlier, this mode may find applications in Synthetic Vision.

### *5.8.2 Honeywell Turbulence Sensor*

The Honeywell sensor (Table 8) operates in a narrow band around 12.2 microns, which can be achieved by specifying an extended wavelength range. The $30° \times 30°$ FOV can also be achieved with custom optics, and the array of smaller fields of view could be emulated by averaging data in appropriate clusters of pixels.

The high data rate of Honeywell's sensor, 100 readings per second, cannot be accommodated by a MIDIS system, but this data rate is not essential for the proposed detection scheme. It is used as a convenience, so that aircraft motion during each sample can be ignored in the data analysis.

#### *5.8.3 CSIRO Multi-Hazard Sensor*

A standard 2000L imager would meet the requirements shown in Table 10 for the CSIRO volcanic ash detector. For $SO_2$ and $H_2SO_4$ (Table 11), an extension of the wavelength range to 7.4 microns would be required. For CAT, CSIRO proposes to use the water vapor band at the lower-wavelength end of the 8 - 12 micron window, so an extension to 6.8 microns would be required, as shown in Table 12. As noted earlier, these shorter wavelength ranges are available as a custom order. For all of the CSIRO sensors, the 2000L reduced pixel format of 128 x 128 would be more than adequate, and the temperature resolution would also be more than adequate. [50]

# 6 Conclusions

For detecting the icing hazard, dual-polarization microwave radiometry emerged as the only potential radiometric technique. This method has been actively investigated during the past two years by means of simulations, and supporting data were acquired in 1999 with a polarimetric radiometer in icing conditions on a mountaintop. The radiometer technology is mature and available, but further simulation and modeling work is required to determine whether radiometric MMW icing sensors are best deployed as airborne or ground-based sensors. This research is currently under way as a Phase II SBIR effort by Radiometrics, Inc. in conjunction with the NASA Glenn Research Center, and related work is being conducted in an on-going research program at NCAR.

For turbulence detection, IR radiometric techniques have been investigated for many years. Current research in this area is being conducted by Honeywell as an internal R&D effort. Honeywell has developed a prototype radiometric sensor and is currently investigating IR techniques with both simulations and flight tests. Turbulence detection by IR radiometry shows great promise, especially in terms of detection range, but significant questions remain to be answered. This technique deserves further investigation.

The technology for radiometric detection of turbulence can be advanced in two ways: with better flight tests and with better simulations. Ultimately, a combination of flight tests and simulations must be used to determine the probability of detection, false alarm rate, and correlation of the sensor output with the severity of turbulence. Future flight tests must include measurements of truth data, including both the temperature structure and the severity of the turbulence. One potential way of acquiring such data sets is to fly an IR sensor in conjunction with the NOAA's SCATCAT tests.

For detection of volcanic ash, the two-band satellite image analysis technique has been adapted for airborne sensing by the Commonwealth Scientific and Industrial Research Organisation (CSIRO) in Australia. Although the technology base for this technique is mature, flight testing to date has been limited, and some developmental work remains to be completed. As suggested by CSIRO, an attractive feature of an IR volcanic ash sensor is its similarity to an IR turbulence sensor. This similarity potentially allows for the development of one radiometric sensor that would warn aircrews of both ash and turbulence. Such a dual-purpose sensor would be more acceptable and affordable to the commercial aviation industry than two separate sensors.

The similarities of the IR hazard detection techniques for turbulence and volcanic hazards suggest that both of them could be emulated with one multi-spectral imaging system. GTRI investigated the availability of suitable commercial IR spectral imagers, and located only one that covered the required spectral region, a hyperspectral imager manufactured by Surface Optics Corporation.

This imager, the MIDIS 2000L, provides data cubes with a 256 x 256 pixel image format and it divides the 7-12 micron spectral range into either 30 or 60 spectral bands, depending on how it is operated. The imager can be purchased with options such as a wider field of view and an extended spectral range.

The ability of the MIDIS 2000L imager to emulate the sensors proposed by Honeywell and CSIRO (as well as other proposed IR imaging sensors) was investigated in detail. The Surface Optics imager, with the correct options and some special features, was shown to be capable of emulating the other proposed sensors. In addition, the imager features a FLIR (Forward-Looking Infrared) emulation mode, so it can also be used as a long-wave imaging system that produces video data. As such, the imager could be used in other NASA programs such as Synthetic Vision. For these reasons, the MIDIS 2000L is the best choice for an instrument to advance the state of the art in IR detection of aviation hazards.

During the course of the work reported here, the inadequacy of the modeling and simulation support for much of the sensor development has become apparent. A much more extensive modeling and simulation capability should be developed, preferably in a government or university environment so that results can be shared with the entire aviation safety community. The data from future flight tests of radiometric hazard detection techniques should be analyzed and understood in the framework of simulation models. Because it is simply not feasible to fly a prototype sensor in all possible conditions, simulation is the only way that crucial questions in regard to probability of detection and false alarm rate can be assessed before a sensor system is actually deployed. Development of such a capability will be an extremely helpful step in getting a radiometric hazard sensor developed and deployed on commercial aircraft.

# Appendix A - The Incident at Redoubt Volcano

The following description of the incident at Redoubt volcano is taken directly from reference [38].

The incident at Redoubt volcano is one of the most famous and dramatic accounts of an airplane entering an ash cloud. The following excerpt, by Campbell, should provide you with an idea of the sense of confusion and panic.

Redoubt volcano, near Anchorage Alaska, began erupting on December 14, 1989. On the following day, a 747-400 airplane powered by GE CF6-80C2 engines entered an ash cloud at 25,000 ft. and experienced flameouts on all four engines.

During descent to 25,000 ft., the airplane entered a thin layer of altostratus clouds when it suddenly became very dark outside. The crew also saw lighted particles (St. Elmo's fire) pass over the cockpit windshields. At the same time, brownish dust with a sulfurous smell entered the cockpit. The Captain commanded the Pilot flying to start climbing to attempt to get out of the volcanic ash. One minute into the high-power climb, all four engines flamed out due to the volcanic ash and dust in the cockpit. The crew donned oxygen masks.

The Pilot Flying noticed the airspeed descending, initially at a normal rate (given the airplane's altitude) but suddenly very fast. All airspeed indications were then lost due to volcanic dust contamination in the pitot system. At the same time, there was a stall warning and the stick shaker was activated with no signs of buffeting. The Pilot Flying rather firmly put the nose of the aircraft down to avoid a stall and initiated a turn to the left in a further attempt to get out of the volcanic ash.

The crew noticed a "Cargo Fire Forward" warning and deduced that the fire warning was caused by the volcanic ash, so no further action was taken.

As the engine spooled down, the generators tripped off and all instrument were lost except for instruments powered by the batteries.

During the time the engines were inoperative, the cabin pressure remained within limits and no passenger oxygen masks deployed. The crew elected not to deploy the masks because the passenger-oxygen-mask system would have been contaminated by volcanic dust in the cabin air.

An emergency was declared when the airplane passed through approximately 17,000 ft. The crew stated that total of seven or eight restart attempts were made before engines 1 and 2 finally restarted at approximately 17,200 ft. Initially, the crew maintained 13,000 ft. with engine 1 and 2 restarted, and, after several more attempts, engines 3 and 4 also restarted.

After passing abeam and east of Anchorage at 11,000 ft, the airplane was given radar vectors for a wide right-hand pattern to runway 06 and further descend to 2,000 ft. The Captain had the runway continuously in sight during the approach; however, vision through the windshields was impaired due to "sandblasting" from the volcanic ash in such a way that the Captain and the First Officer were only able to look forward with their heads positioned well to the side. Finally the airplane did land safely, but approximately 80 million dollars was spent to restore the plane, which included replacing four engines. The in-depth account of this incident helped researchers devise a procedure of what a crew should do when they encounter an ash cloud.

# Appendix B - Icing

## Phenomenology of Icing

Aircraft icing occurs in clouds with significant liquid water content at temperatures below 0 °C. However, not all such clouds present a serious hazard to aviation. Between 0 °C and –40 °C there are four temperature regimes where icing is either insignificant or has a minimal effect on aircraft performance. These regimes are:

Regime 1: at temperatures T > -2 °C, water freezes slowly and can coat the airfoil with a glass-like glaze called "Rime" ice. Icing of this type can be handled with de-icing equipment.

Regime 2: at temperatures T < -15 °C, water freezes quickly on the wing's leading edge.

Regime 3: at temperatures T < -20 °C, clouds consist mostly of ice particles with a small admixture of SLD,

and Regime 4: at temperatures T < -40 °C, clouds are composed entirely of ice crystals.

Given the above non-hazardous temperature regimes, the temperature region that is of concern for the aviation icing hazard is between –4 °C and –10 °C, lying between regimes 1 and 2. [22] This hazard region is sometimes extended to the range between 0 °C and –20 °C [51], which spans the freezing level composite generated every fifteen minutes by the Aviation Weather Center in Kansas City, MO. The composite is a 4km resolution mapping of the entire US showing radar returns from clouds centered at the –10 °C temperature level. [10]

It has been suggested [52] that due to the temperature change with altitude, icing conditions should exist in only a relatively thin layer in the atmosphere. However, Rauber and Grant found preferred regions for Super-cooled Liquid Water (SLW) in stratiform clouds, in cloud tops, and in cloud base regions. [53] Politovich [54] has compiled normalized vertical profiles of SLW from the Winter Icing and Storms Project (WISP94) data, which indicates a distribution of SLW throughout the vertical cloud extent. Therefore, no preferred location for SLW within a cloud exists. Furthermore, given the SLW formation mechanisms and the convection currents in clouds, SLW can be encountered anywhere within the cloud volume.

*A priori* knowledge of the cloud type in which icing is most likely to occur coupled with cloud temperature profiling has been considered for a simple and inexpensive detection system using a temperature profiling radiometer. However, cloud type and temperature profiles are not reliable indicators of icing conditions, and can provide misleading results when used in place of direct icing detection. [11] The complexity of cloud micro and macrophysics, due to the presence of localized conditions, can rapidly convert a benign cloud to one that contains icing hazards.

Another complicating factor for detection of icing conditions is the presence of mixed phases in clouds. Above 0 °C, all cloud particles are droplets of liquid water. Between 0 °C and about –40 °C, a cloud can be in a mixed phase that includes both SLW and ice crystals. The presence of mixed phases means that knowledge of a cloud's temperature and water content is insufficient to determine whether it presents an icing hazard. It is necessary to determine that it contains SLW, which is especially hazardous as the drizzle-sized droplets known as SLD. For all types of remote sensing measurements, the characteristic signatures and the specific contributions of each phase must be considered so the SLW phase can be discriminated from the benign liquid water and ice crystal phases.

### *FAA Regulations*

For aircraft icing, the size of the SLW drops is very important, as described above. The most dangerous SLW is drizzle size droplets, which are about 100 microns in diameter. [10][55] There is a direct correlation between liquid water content (LWC) and mean droplet diameter. Consequently, FAA regulations have two sets of conditions, which define an envelope within which the FAA requires hazard identification and certification for icing. [54][56][57]

| | |
|---|---|
| 1st set of Conditions: Detect | LWC = ~ $0.1 g/m^3$<br>Cloud Drop Size diameter (d) as small as 15 microns |
| 2nd set of Conditions: Detect | LWC = ~ $0.6 g/m^3$<br>d = 15 - 59 microns |

It is expected that the FAA will extend the envelope sometime in the future to include:

LWC > $0.2 g/m^3$
d = 50 microns to 1 mm

At this time, this envelope is used for certification of aircraft de-icing systems, not as a specification for detection of icing conditions. The FAA regulations are mentioned here because any future commercial icing detection system will have to operate in this regulatory environment. [56]

# Appendix C - Clear Air Turbulence

## Causes of Turbulence

Mountain-induced turbulence occurs when an air mass encounters the side of a mountain. [18] The air mass is forced upward into a region where the air is less dense due to the higher altitude. Because this air mass is now denser than the surrounding air, it consequently falls back down below its original height. Now the air mass is less dense than the surrounding air, and it rises again, etc. A buoyancy force causes the mass to continue in this oscillating pattern; therefore, this oscillating air mass is called a buoyancy wave, or gravity wave. [58][59] This cycle generates turbulence that is felt above mountain ranges and downwind from the ranges as well. [18]

Gravity waves are formed in the troposphere by mechanisms other than mountain ranges. Storm systems and the jet stream can also cause gravity waves. As gravity waves propagate, they carry momentum and heat through the troposphere. [59]

CAT occurs at the edges of the jet stream due to the Kelvin-Helmholtz instability, in addition to gravity waves. This instability is caused by the shearing effect of a faster air current moving next to a slower air current. [60] CAT also occurs due to the convective turbulence of stormy skies. Convective turbulence can create disturbances 20 miles away, where there are no clouds, making it difficult to detect. [18]

## Kuhn and Sinclair 'S' Layer Model

In the early 1990's, Kuhn and Sinclair developed an 'S' layer model to describe the wave instabilities that lead to CAT. [24] The 'S' layer is comprised of 3 layers that form an 'S' shape on a graph of altitude (Z) vs. temperature (T), as shown in Figure 3. [24]

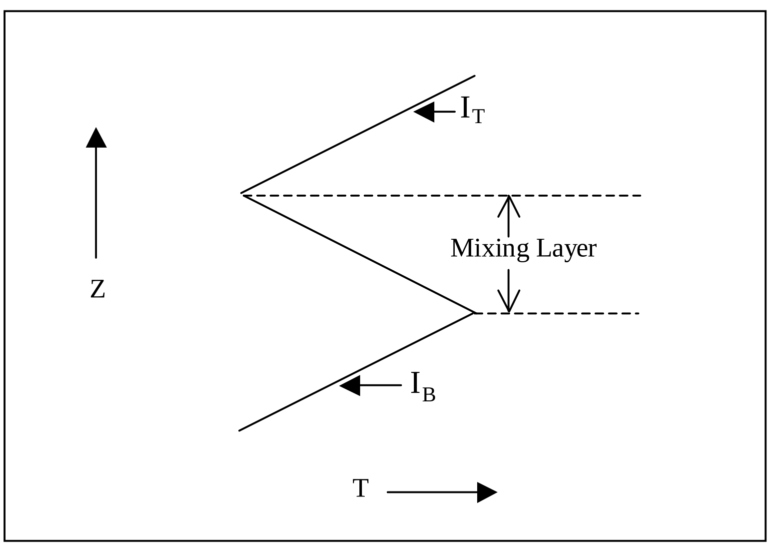


Figure 3. 'S' layer depiction derived from Kuhn and Sinclair.

The mixing layer is the region where the initial growth of the instability occurs. $I_T$ and $I_B$ are the inversion layers that bound the energy of the instability within the mixing layer, allowing CAT growth.

The model was flight tested by the Air Force at 45,000-70,000 ft with U-2 aircraft during the High Altitude Clear Air Turbulence (HICAT) program, which took direct measurements of full gust velocity, wind, temperature, and height. Table 18 [24] gives the correlation between CAT and the 'S' Layer model. In 18 out of 19 cases where the 'S' Layer was detected, so was CAT, whereas in 43 of 46 cases where no 'S' Layer was detected, no CAT was detected either. These results give a 93.8% forecast capability for the 'S' Layer model. And, as expected from the model, in the 18 cases where CAT was observed in the 'S' Layer, it was located in the mixing layer in 100% of the cases and in the inversion layers in 33% of the cases. In no case was CAT located in the inversion layers without being found in the mixing layer as well. [24]

Table 18. 'S' Layer CAT Contingency

| 'S' Layer CAT | CAT | No CAT | Total | % Verification |
|---|---|---|---|---|
| 'S' Layer | 18 | 1 | 19 | 94.7 |
| No 'S' Layer | 3 | 43 | 46 | 93.5 |
| Total | 21 | 44 | 65 | 93.8 |

## Honeywell Model

For purposes of illustration, the atmosphere is considered to be horizontally stratified, with laminar flow both above and below an intermediate layer. The wind directions and/or speeds are different at the two altitudes, as shown in Figure 4, taken from reference [28].

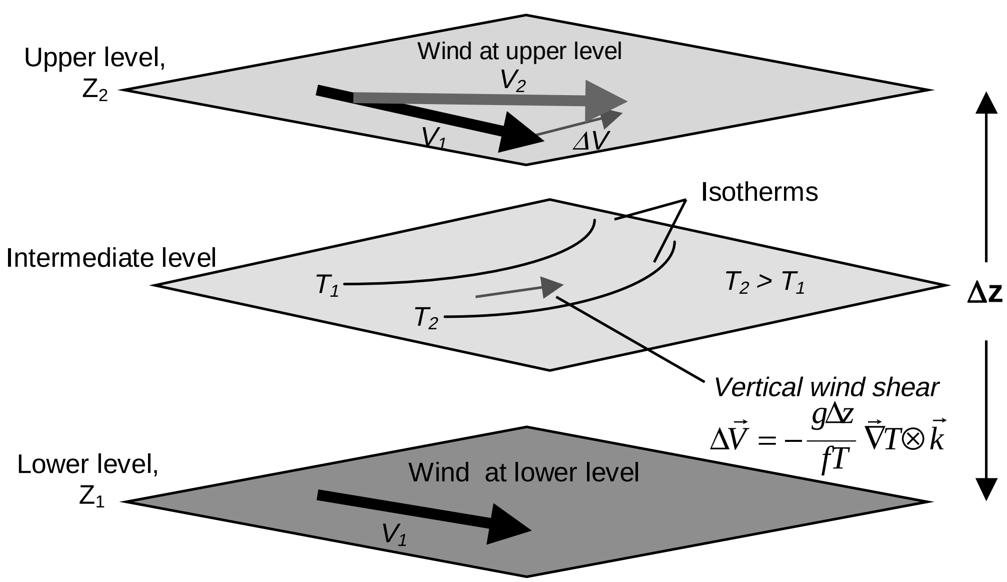


Figure 4. The relationship between vertical wind shear and temperatures in the intermediate layer.

The algorithm for calculating the wind shear $\Delta\vec{V}$ is given in Figure 4. Here, g is the acceleration due to gravity, $\Delta Z = Z_2 - Z_1$, f is the coriolis parameter due to the earth's rotation, $\vec{\nabla}T$ is the horizontal temperature gradient in the intermediate level, and $\vec{k}$ is the unit vector parallel to the local vertical.

Note that the algorithm for calculating wind shear requires a two-dimensional map of atmospheric temperatures. Temperature data is obtained by a calibrated radiometer, and spatial coverage is obtained by combining the aircraft's forward motion with azimuthal scanning. A passive sensor does not measure at a specific range, but an effective range, $R_{eff}$, can be defined as

$$R_{eff} = \frac{\sum_{0}^{\infty} L_r R_r}{\sum_{0}^{\infty} L_r}$$

where $L_r$ is the radiance received from a parcel of air at the distance $R_r$. The effective range is expected to be large, typically 70 to 120 km at cruising altitude, and the anticipated scanning angles will be sufficient to sample a swath of air 200 km wide.

In April 1997, Honeywell performed a 13-day flight test at an altitude of 13,040 feet. Wind speeds and directions calculated from the IR radiometer data were compared with radiosonde data, with the following results:

1) The concept of effective range and temperature measurements was demonstrated.
2) Wind shear at 18,800 feet was accurately predicted.
3) Real-time capability of the passive IR method was demonstrated.

Honeywell has also done extensive simulations of their proposed detection technique using the IR radiative transmittance model FASCODE and the Evergreen data set from NCAR. These simulations gave promising results.

# Appendix D - Volcanic Ash

## Two-Band IR Method

The two-band IR method utilizes a pictorial analysis known as the Brightness Temperature Difference (BTD) to distinguish volcanic clouds from meteorological clouds. The ash clouds are distinguishable from meteorological clouds, because the ash clouds have a negative BTD, while meteorological clouds have a positive BTD. [33][61][62] The BTD is calculated by subtracting the digital-image radiance data of band 5 (11.5-12.5 μm) from the radiance data of band 4 (10.5-11.5 μm), where bands 4 and 5 are channels of the Advanced Very High Resolution Radiometer (AVHRR). [33][61][62]

Meteorological clouds can be opaque or transparent. In either case, meteorological clouds will always have a positive band 4 minus band 5 BTD; in fact, most components of the earth's surface have a positive band 4 minus band 5 BTD. [61] When the cloud is opaque, the cloud absorbs all of the thermal energy from the area underneath the cloud. The satellite sensor only detects the energy that is radiated from the cloud, which results in a positive BTD. [61] For transparent meteorological clouds, the sensors detect a combination of the cloud's radiance and that of the underlying area. Due to greater refractive indices of ice and water in the band 5 region, more energy from the underlying area is absorbed in the band 5 region, creating a positive band 4 minus band 5 BTD. [61]

Volcanic ash clouds can be opaque or transparent as well. The opacity of the ash clouds changes as the cloud ages, becoming more transparent with time. Younger ash clouds contain larger amounts of water and ice, giving them similar BTDs to meteorological clouds. As the cloud ages, it dries out, with the leading edges drying out first, giving the cloud an outline of negative BTD values. [33][61] The negative BTD occurs because of the greater refractive index of silicates in the band 4 region; therefore, more energy is absorbed in the band 4 region. [61] Figure 5, taken from reference [61], is a pictorial explanation of the absorption and the resulting BTD that occurs in a transparent volcanic cloud.

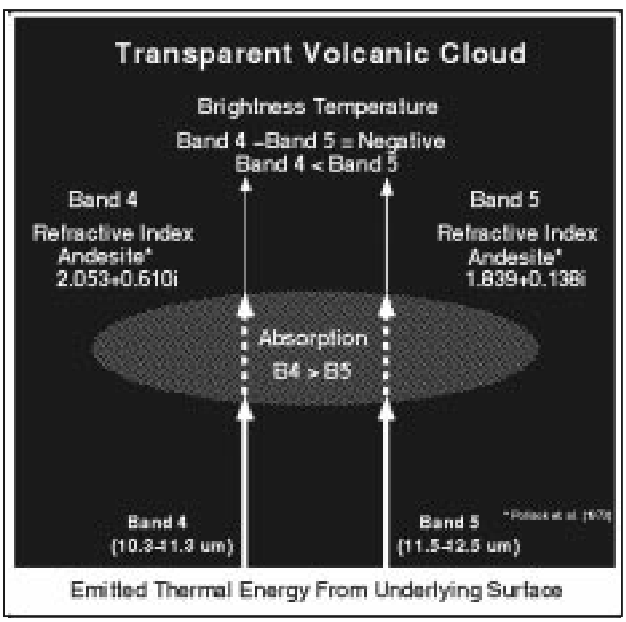


Figure 5. Representation of absorption and the BTD in a transparent volcanic cloud.

Figure 6, also taken from reference [61], demonstrates the two-band IR method through images of the Mt. Spurr cloud. The image on the left shows a band 4 image, while the image on the right is a band 4 minus band 5 image. The volcanic cloud is easily distinguished from the meteorological clouds in the right-hand image.

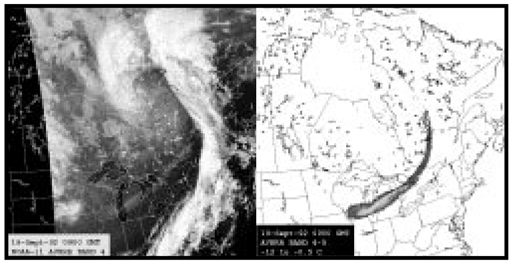

Figure 6.  Demonstration of the two-band IR method.

Other methods of detection are being investigated. For example, Frederick Mosher at the Aviation Weather Center is investigating a method that builds on the two-band method. His four-band method does detect the volcanic ash, but is hampered by the detection of thin cirrus clouds as well. [63]

# Appendix E - MIDIS Performance Specifications [49]

## MIDIS Imaging Modules

The following sections summarize the specifications of the MIDIS 2000M, 2000L, and 2000P hyperspectral imaging collection and real-time processing system.

### *Design Philosophy*

The MIDIS instrument is intended to be a multi-band, real-time imaging spectroradiometer. Rather than simply provide raw imagery that the user then needs to calibrate and process, MIDIS incorporates all stages of processing (calibration, atmospheric correction, sensor emulation, and spectral correlation) to allow real-time extraction of information from hyperspectral image cubes generated by the imaging modules. Raw data can also be stored for future analysis or processing, allowing tremendous flexibility in data collection and exploitation.

### *Spectral Scanning Technique*

The MIDIS imaging modules employ multi-slit, prism-based imaging spectrometers for spectral image generation. Using a prism provides band-simultaneous acquisition of spectral imagery, ensuring that no spectral distortion of imaged items occur. Such spectral distortion, inherent in band-sequential systems such as liquid crystal tunable filters, acousto-optic tunable filters, Fourier transform, circular and linear variable filters, destroys an object's true spectral signature when that object moves relative to the sensor during a cube acquisition period. Prisms also provide extremely high throughput, limited mainly by the reflection losses at the interfaces. Gratings, on the other hand, can provide reasonably high peak efficiency (as much as 80%), but fall off to about half that level on either side of the peak (over an octave range). Gratings are also limited to one octave of wavelength coverage, without order-sorting filters. Since MIDIS uses multiple slits to increase temporal resolution, use of an order-sorting filter for the MWIR is problematic.

### *Spectral Coverage*

The MIDIS 2000L, the LWIR imaging module, covers the spectral range from 8 – 12 μm, covering the majority of the LWIR atmospheric window.

The MIDIS 2000M, the SWIR/MWIR imaging module, covers the spectral range from 2.0 – 5.0 μm, providing coverage of the 2.0 – 2.5 μm and the 3.0 – 5.0 μm atmospheric windows.

### *Spectral Resolution*

The MIDIS 2000L provides the following spectral resolutions:

0.14 μm @ 10 μm for 30 band implementation
0.068 μm @ 10 μm for 60 band implementation
Bandwidth variation across the 8 – 12 μm band is less than 1.8 to 1

The MIDIS 2000M provides an approximate spectral resolution of:

0.10 μm @ 3.5 μm for 30 band implementation
0.05 μm @ 3.5 μm for 60 band implementation
Bandwidth variation across the 2 – 5 μm band is less than 1.5 to 1

Note that numbers stated for the 2000L are based on a finalized design, whereas the 2000M are based on a design in progress. Hence, the latter numbers may change slightly, but not significantly.

***Temporal Resolution***

The MIDIS 2000L provides variable temporal resolution with cube rates as follows:

| | |
|---|---|
| 256 x 256 spatial x 30 spectral: | 3.75 cubes per second |
| 128 x 256 spatial x 30 spectral: | 7.5 cubes per second |
| 128 x 128 spatial x 30 spectral: | 15 cubes per second |

Frame rates are half for 60-band mode. The system SNR for both 30 and 60-band operation viewing a 300K grassy field through a 1 km atmospheric path are shown in Section 3.25. [Not a part of this document]

The MIDIS 2000M incorporates a higher frame-rate imager, providing better temporal resolution as follows:

| | |
|---|---|
| 256 x 256 spatial x 30 spectral: | 15 cubes per second |
| 256 x 256 spatial x 60 spectral: | 7.5 cubes per second |

The SNR data for the same conditions as above is presented in Section 3.25.

***Validation***

Both the MIDIS 2000L LWIR and MIDIS 2000M SWIR/MWIR imaging modules are new products, currently in manufacture and design, respectively. The LWIR unit has been reviewed by the imaging technology group of Boeing Space & Defense Systems in Anaheim, CA, who concluded that the design was good and would function as stated. Further reviews have been performed by two other optical houses, including the one currently manufacturing the system, also showing the design will function as stated. The MWIR imaging module design is nearing completion and will also be reviewed by Boeing and other outside vendors prior to manufacture to ensure proper function.

***Growth Capabilities***

Since the MIDIS 2000P common processor is based on a modular concept, users can readily add the VIS/NIR hyperspectral imaging module whenever desired, which provides coverage from 0.4 – 1.0 μm. Additionally, since the processor is reconfigurable, new algorithms can be developed and added as required. Similar reconfigurability is included in the electronics in the hyperspectral imaging modules, allowing updates to enhance their performance to be easily implemented when available. Finally, interchangeable fore-optics allow changing the FOV and IFOV when required, although this is contingent on availability of alternate fore-optics, or on a custom development.

***Flexibility***

The MIDIS system offers excellent flexibility in both image acquisition and processing. Frame rates delineated in Section 3.5 [Not a part of this document] are maximum rates. Frame rates can be decreased for increased sensitivity. As shown in Section 3.5, the LWIR imager also offers a trade-off between spatial and temporal resolution. Using either 30 or 60 bands, trade-off between spectral and temporal resolution is also possible. Extreme flexibility also exists in the 2000P processor. Since the hardware is reconfigurable through software, algorithms can be changed on the fly and new algorithms can readily be implemented.

### *Aircraft Operability*

The MIDIS instrument can be used in an aircraft in two different modes. First, it can be used as a full frame imager, looking in any direction relative to the aircraft's motion. Second, MIDIS's scan mirror can be stopped, allowing the system to operate as a push-broom imager, using the aircraft's forward motion to generate one spatial dimension. Note that especially in the push-broom mode, some degree of imager stabilization may be required.

### *Instantaneous Field of View*

The current 2000M and 2000L IFOV with the standard 50 mm focal length lens is 800 μrad.

### *Minimal Focal Distance*

The minimum object distance (MOD) for the MIDIS 2000M and 2000L is 1.6 m.

### *Optics F-Number*

The 2000M and 2000L spectrometers consist of a three-lens system: the fore-optics, the collimating lens (after the slit plane and before the prism) and the reimaging lens (after the prism). The fore-optics is a 50 mm lens. Each of the spectrometer optics is a 60 mm lens.

All optics have a relative aperture of f/1.75.

### *Optics Transmission*

Total optics transmission of the 2000M and 2000L averages approximately 48%.

### *Data Cube Storage*

Two data cube storage options are available. The first is capable of storing 4,900 cubes of 256 x 256 x 60. The second is capable of storing 9,800 cubes of 256 x 256 x 60. This storage is available in real-time and corresponds to 9 minutes of recording, for the first case, if both imaging modules are producing data at their maximum rate. For the second case, storage time is 18 minutes at the maximum data rate.

Even larger recorders are available at additional cost.

### *Data Cube Storage System*

Each of the two storage options listed in Sections 1.14 [Not a part of this document] is a RAID system. The first option contains 36 GB of storage; the second contains 72 GB. Each also includes a high-speed data port for formatting data written to the storage arrays, allowing hyperspectral imagery to be streamed directly to the storage array for real-time recording.

### *Dimensions*

The 2000M and 2000L imaging module size (excluding Processor) is 15cm x 20cm x 50cm.

### *Weight*

Imaging Module Weight (excluding Processor): < 12kg

***Power***

Imaging Module Power (excluding Processor) Requirement: < 75W

***Detector Material***

Both spectral imaging modules use Mercury-Cadmium-Telluride (HgCdTe) arrays, one tailored for a 5 µm cutoff, the other for a 12 µm cutoff.

***Detector Sensitivity***

Detector detectivity, $D^*$, being an extrinsic rather than intrinsic detector property, can be a difficult parameter to use to accurately specify a detector's performance. Detectivity does includes intrinsic parameters such as quantum efficiency, read-noise and dark current, but also includes the irradiance on the detector, a function not of the detector, but of the optical system and environment that the detector is in. As such, detectivity must be quoted under very specific conditions. Further information on relationship of intrinsic detector properties and detectivity can be supplied on request. Quoted below are the intrinsic performance limiting parameters for MIDIS's FPAs. If additional information is required, $D^*(\lambda)$ can be generated for various operating conditions.

<u>LWIR FPA</u>

| | |
|---|---|
| Quantum Efficiency: | > 60% |
| Read-Noise: | < 600 $e^-$ |
| Dark Current: | < 5 x $10^9$ $e^-$/s (@ 77K) |
| Charge Capacity: | > 4 x $10^7$ $e^-$ |

<u>MWIR FPA</u>

| | |
|---|---|
| Quantum Efficiency: | > 60% |
| Read-Noise: | < 250 $e^-$ |
| Dark Current: | < 1 x $10^6$ $e^-$/s (@ 77K) |
| Charge Capacity: | > 2 x $10^6$ $e^-$ (in standard gain mode) |
| Charge Capacity: | > 3 x $10^5$ $e^-$ (in ultra-high gain mode) |

***Detector Format***

Both the SWIR/MWIR and LWIR imaging modules use FPAs of 256 x 256 size.

***Detector Dynamic Range***

The LWIR array exhibits a dynamic range, full well capacity divided by the RMS read-noise, of nearly 70,000. Including statistical variations in integrated dark current over a 5 ms integration time yields a dynamic range of greater than 8,000.

The MWIR array exhibits a noise-limited dynamic range of 8,000. Dark current variations over a 5 ms integration time decrease this value minimally.

***Detector Cooling***

Both arrays and optical systems are cooled using $LN_2$.

### *Calibration*

All pixels in the arrays are independently calibrated both spectrally and spatially, first using a laboratory calibration source, then periodically by viewing an internal reference source. Calibration also corrects offset levels caused by dark current and background radiances independently at each pixel. Output from the Frame Interface and Calibration (FIAC) card in the processor is calibrated spectroradiometric imagery, not just raw digital values.

### *SNR*

The following charts show the system SNR for both 30 and 60 band operation viewing a 300K grassy field through a 1 km atmospheric path, for both the LWIR and SWIR/MWIR imaging modules.

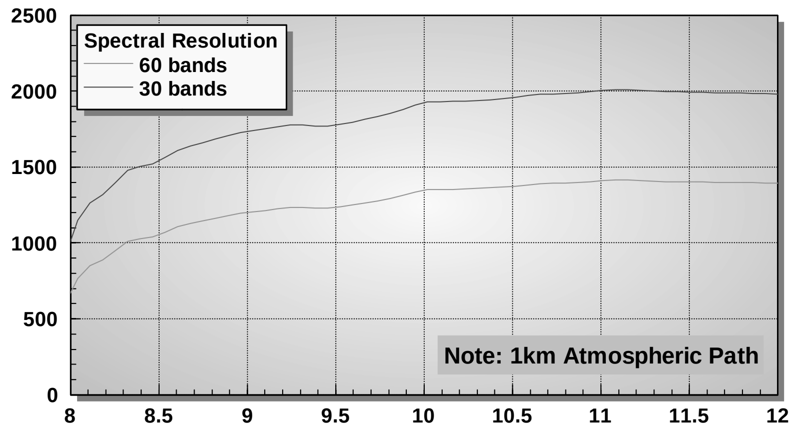


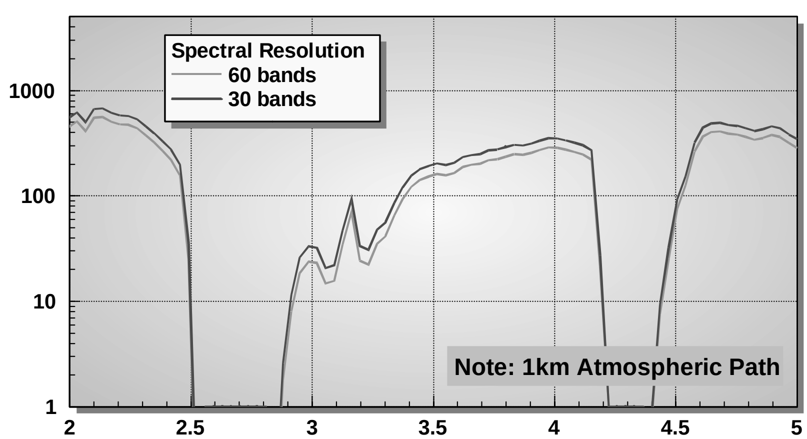


### *Data Resolution*

Data out of the detectors is digitized to 12 bits. A minimum of 16 bits is maintained throughout processing, with actual data width depending on processing being performed (an advantage of re-configurable hardware). One algorithm uses 50 bits of resolution at one point in the processing. Adequate data width is maintained to ensure no precision is lost during the processing.

All source code, in Visual C++ 6.0 and assembly, will be made available to the customer. SOC will support the customer in minor modifications to the code, if so required.

### *Software Updates*

SOC will provide software upgrades for the MIDIS 2000M/L/P to the customer for a minimum of three years.

### *Real-time Spectral Image Processing*

Data from the two hyperspectral-imaging modules is fed to the MIDIS 2000P real-time hyperspectral image processor. This processor allows treating the data from the two imaging modules as if it had come from one, providing spectra from 2 to 12 μm. This processor implements spectroradiometric calibration, atmospheric correction, sensor emulation, and spectral correlation all in real-time. Spectral correlation allows highlighting or suppressing objects based on spectral signatures, the results of which can be overlaid on any or all of the three sensor emulation channels. This provides a means to present an image that a user would be familiar with, e.g., a broad-band FLIR emulated image, with regions in it highlighted based on the results of the spectral processing.

### *Atmospheric Correction*

The pre-processor module of the MIDIS 2000P provides for real time correction of atmospheric gas absorption and emission, and aerosol scattering, absorption, and emission. The reconfigurable atmospheric correction algorithms are currently based on work done by Caltech's Jet Propulsion Laboratories as embodied in ATREM. Surface Optics is currently working with Spectral Sciences, Inc., a leader in development of hyperspectral image processing algorithms, to further refine the atmospheric correction algorithms implemented by the MIDIS 2000P processor.

# Appendix F - Other Sources Found in the Literature Search

GTRI has conducted a literature search on work related to radiometric detection of aviation hazards. This search included the National Technical Information Service (NTIS), INSP, the Department of Defense Classified (DTIC) databases, and the World Wide Web. Useful sources of information that are not specifically referenced in this report are listed below.

Icing:

Stankov, B. B. and A. J. Bedard, Jr., 1994: Remote Sensing Observations of Winter Aircraft Icing Conditions: A Case Study. *Journal of Aircraft*, Vol. 31, No. 1 Jan-Feb, pp.79-89.

Stankov, B. B., B. E. Martner, M. K. Politovich, 1995: Moisture Profiling of the Cloudy Winter Atmosphere Using Combined Remote Sensors. *Journal of Atmospheric and Ocean Technology*, Vol. 12, pp.488-509.

Rasmussen, R., M. Politovich, J. Marwitz, W. Sand, J. McGinley, J. Smart, R. Pielke, S. Rutledge, D. Wessly, G. Stossmeister, B. Bernstein, K. Elmore, N. Powell, E. Westwater, B. Stankov, and D. Burrows, 1992: Winter Icing and Storms Project. Bull. Amer. Meteor. Soc., 73, 951-974.

Additional information on SLW droplets and their mixed phase with ice crystal can be formed in http://www.phys.ufl.edu/~peterson/chap8/chapter8.html

Ashenden, R., W. Lindberg, and J. Marvitz, 1996: Two-dimensional NACA 23012 Airfoil Performance Degradation by Super Cooled Cloud, Drizzle, and Rain Drop Icing. American Institute and Astronautics paper 06-0870.

Politovich, M. K.1989: Aircraft icing caused by large super cooled droplets. J. Appl. Meteorol. 28. pp.856-868.

Gasiewski, Dr. Albin, NOAA-ETL, Private communications, 2000.

Popa Fotina, I. A., J. A. Schroeder, and M. T. Decker, 1986: Ground-based detection of aircraft icing conditions using microwave radiometers. IEEE Trans. Geosci. Remote Sens., GE-24, 975-982.

Marshall, Robert E., Mark A. Richards, Joe A. Galliano, Jorge Montoya, 1993: Advanced Microwave Sensing Technology Study For Civil Aviation Atmospheric Hazards. NAS1-18925, Task Assignment No. 23.

Clear Air Turbulence:

Sinclair, P. C. and Kuhn, P. M.: An Airborne FLIR Detection and Warning System for Low Altitude Wind Shear. *Journal of Applied Meteorology*, November, 1990.

Sinclair, P. C. and Kuhn, P. M.: Airborne Infrared Wind Shear Detector Performance in Rain Obscuration. 25th Aerospace Sciences Meeting. January 12-15, 1987, Reno, Nevada. Published by American Institute of Aeronautics and Astronautics, Inc.

FAA, NASA to Test Turbulence Detection Devices. Air Bulletin. http://www.airconnex.com/bulletin/back/2-01-09.html Accessed June 22, 2000.

Henderson, Sammy: Doublet-Pulse Wind Field Sensor. Coherent Technologies, Inc. http://www.navysbir.brtrc.com/SuccessStories/CoherentP3.html Accessed June 22, 2000.

Volcanic Ash:

Casadevall, Thomas: Volcanic Ash and Aviation Safety: Proceedings of the First International Symposium on Volcanic Ash and Aviation Safety. 1994. http://vulcan.wr.usgs.gov/Glossary/Tephra/Bulltin2047/foreword.html Accessed June 16, 2000.

Wright, and Pearson: Living with Volcanoes: The USGS Volcano Hazards Program. Danger in the Stratosphere: Aircraft and Volcanic Plumes. 1992. http://vulcan.wr.usgs.gov/Vhp/C1073/aircraft_plumes.html Accessed June 16, 2000.

Rose, William; Bluth, Gregg; Coke, Larry; Kostinski, Alexander; Perger, Warren: Volcanic Cloud Remote Sensing Group. Laboratory of Atmospheric Remote Sensing. Michigan Technological University. http://www.geo.mtu.edu/~raman/volccloud.html Accessed June 16, 2000.

Prata, A. J.; Barton, I. J.: Hazard from Volcanic Ash. *Nature*, Vol. 354, November 7, 1991, p. 25.

Prata, A. J.; Barton, I. J.: Detection and Discrimination of Volcanic Ash Clouds by Infrared Radiometry – I: Theory. Volcanic Ash and Aviation Safety: Proceedings of the First International Symposium on Volcanic Ash and Aviation Safety. U.S. Geological Survey Bulletin 2047. p. 305-311.

# References


[1] Office of System Safety Weather Study. Total Accidents/Weather Accidents Comparison. http://www.asy.faa.gov/safety_analysis/weather_study/totals.htm Accessed 1/9/01.

[2] Office of System Safety Weather Study. Bureau of Transportation Statistics - Airline Traffic Statistics; Cautions About The Analysis Of Aviation Safety Data. http://www.asy.faa.gov/safety_data/#hints Accessed 1/11/01.

[3] Office of System Safety Weather Study. NTSB Weather Related Accidents by FAR Part. http://www.asy.faa.gov/safety_analysis/weather_study/parttb.HTM Accessed 1/9/01.

[4] AT Special Reports – ICAO Universal Safety Oversight Audit Programme. http://www.aviationtoday.com/reports/faa_audit04.htm Accessed 1/9/01.

[5] Office of System Safety. Search Screen Element Definitions. Category of Operation. http://nasdac.faa.gov.asy_internet/asy_definitions.htm Accessed 1/9/01.

[6] Private communication with Bill Rose. December 2000.

[7] www.geo.mtu.edu/department/classes/ge404/gcmayber/historic.html Accessed 1/9/01.

[8] Air Transport Action Group (ATAG). Geneva, Switzerland. Asia/Pacific Air Traffic Growth & Constraints. http://www.atag.org/ASIA/Index.htm Accessed 1/10/01.

[9] Nelson, Stephen A.: Tulane University. Geology 212. Igneous Rocks of the Convergent Margins. http://www.tulane.edu/~sanelson/geol212/converg_margins.htm Accessed 1/10/01.

[10] Mosher, F.R. and Lewis, J.S.: Freezing Level Composite of WSR-88D Data for Aircraft Icing Detection, The Aviation Weather Communications – The Aviation Weather Center Newsletter, October 5 1999. http://www.awc-kc.noaa.gov/publications/papers.html Accessed May 30, 2000.

[11] Politovich, M. K.: National Center for Atmospheric Research, Boulder Colorado. Private communications. June 14, 2000.

[12] Kropfli, R. A, et al., 1988: Radar and radiometer measurements of the physical parameters of clouds and precipitation at the NOAA Environmental technology Laboratory, Hanscom AFB, Massachusetts December 1-3. 8pp.

[13] Politovich, Marcia K., J. T. Riley, 2000: Mixed-Phase Icing Conditions. Ninth Conference on Aviation, Range, and Aerospace Meteorology, Orlando Florida, pp.274-279.

[14] Albin Gasiewski NOAA, Private communications, Boulder CO. September 26-27,2000.

[15] Frederic Solheim RADIOMETRICS, and J. Vivekanandan NCAR, Private communications, Boulder CO. September 26-27, 2000.

[16] Solheim, Fredrick, Vladimir Irisov, Vladimir Leuski, Marian Klein, 2000: Airborne Remote Sensing of the Super-Cooled Water and Temperature Environment. NAS3-00051.

[17] Reinking, Roger F. and Robert A. Kropfli, September 2000: Breakthroughs in Radar Polarization Technology and Related Studies. In-flight Icing PDT Technical Direction FY2000 Year-end Task Progress Report to the FAA, Deliverable 00.4.3.E1.

[18] Cowen, Ron: Clearing the Air about Turbulence. Science News Online. Vol. 153, No. 26, June 27, 1998. http://www.sciencenews.org/sn_arc98/6_27_98/bob1.htm p. 408. Accessed June 22, 2000.

[19] NASA & the FAA. A Technology Partnership for the New Millennium. Safety. http://aero-space.nasa.gov/library/nasao/adds.htm Accessed June 22, 2000.

[20] Kenitzer, Stephanie: NOAA to Study Atmosphere Over Pacific Ocean to Improve Weather Predictions and Clear Air Turbulence Forecasts. January 12, 1999. http://www.publicaffairs.noaa.gov/stories/sir46.html Accessed June 2, 2000.

[21] Cecilia Girz, Personal Communication via fax, email, phone, and in person, Oct 2000 – Feb 2001.

[22] Mel Shapiro, NOAA, Private communication, September 27, 2000.

[23] Weaver, E. A.; Ehernberger, L. J.; Gary, B. L.; Kurkowski, R. L.; Kuhn, P. M.; Stearns, L. P.: The 1979 Clear Air Turbulence Flight Test Program.

[24] Sinclair, P. C. and Kuhn, P. M.: Infrared Detection of High Altitude Clear Air Turbulence. 31st Aerospace Sciences Meeting & Exhibit. January 11-14, 1993, Reno, Nevada. Published by American Institute of Aeronautics and Astronautics, Inc.

[25] Feasibility Study of Radiometry for Airborne Detection of Aviation Hazards - Subtask 1. Gary G. Gimmestad, Chris D. Papanicolopoulos, Mark A. Richards, Donald L. Sherman, and Leanne L. West. July, 2000.

[26] Mike Shand, Honeywell, private communication on July 6, 2000.

[27] Mike Shand and Ken Leslie, Honeywell, Private communication, October 4-5, 2000.

[28] "Passive IR Turbulence Detection", Honeywell Technology Center, Morristown, New Jersey, July 2000, Mike Shand and Ken Leslie. This Power Point presentation was furnished by Mike Shand.

[29] Simkin, Tom: Volcanoes: Their Occurrence and Geography. 1994. http://vulcan.wr.usgs.gov/Glossary/Tephra/Bulletin2047/Simkin/abstract.html Accessed June 16, 2000.

[30] Neal, Christina; Casadevall, Thomas; Miller, Thomas; Hendley, James; and Stauffer, Peter: U.S. Geological Survey Fact Sheet 030-97. Volcanic Ash – Danger to Aircraft in the North Pacific, 1997. http://wrgis.wr.usgs.gov/fact-sheet/fs030-97/ Accessed June 16, 2000.

[31] Meyers, Bobbie; Brantley, Steven; Stauffer, Peter; and Hendley, James: What are Volcano Hazards? 1997. http://vulcan.wr.usgs.gov/Hazards/Publications/FS002-97/FS002-97.html Accessed June 16, 2000.

[32] Constantine, Emily ; Maxson Melissa; and Sobczynski, Kristina; Volcanoes, Atmosphere, and Climate. The Dynamics and Implications of Volcanic Eruption Products in the Atmosphere. http://bigmac.civil.mtu.edu/home/classes/ce459/public/p14/clouds.html Accessed June 5, 2000.

[33] Casadevall, Thomas; Delos Reyes, Perla; and Schneider, David: The 1991 Pinatubo Eruptions and Their Effects on Aircraft Operations. http://pubs.usgs.gov/pinatubo/casa/index.html Accessed June 2, 2000.

[34] Dvorak, Joe: Volcano World. Ask a Volcanologist. What is the Elemental Composition of Volcanic Ash from Various Volcanoes? http://volcano.und.nodak.edu/vwdocs/frequent_questions/grp1/question2954.html Accessed June 19, 2000.

[35] USGS Volcano Hazards Program. Volcanic Gasses and Their Effects. http://volcanoes.usgs.gov/Hazards/What/VolGas/volgas.html Accessed June 19, 2000.

[36] USGS Volcano Hazards Program. Danger to Aircraft from Volcanic Eruption Clouds. What can volcanic ash do to aircraft? http://volcanoes.usgs.gov/Hazards/Effects/Ash+Aircraft.html Accessed June 16, 2000.

[37] CEOS Disaster Information Server. Volcanic Hazards. Volcanic Ash Cloud Aircraft Damage. http://www.ceos.noaa.gov/CEOS1/casestud/volcano/plane1.htm Accessed June 5, 2000.

[38] Mayberry, Gari: Natural Hazards Mitigation GE404. Volcanic Ash Clouds and Aircraft Safety. April, 1998. http://www.geo.mtu.edu/department/classes/ge404/gcmayber/intro.html Accessed June 16, 2000.

[39] Slater, David with CSIRO: Personal Communication by FAX. Commercialising the AHDS Technologies. June 7, 2000.

[40] Prata, A. J.; Barton, I. J.: "Detection and Discrimination of Volcanic Ash Clouds by Infrared Radiometry – II: Experimental." Volcanic Ash and Aviation Safety: Proceedings of the First International Symposium on Volcanic Ash and Aviation Safety. U.S. Geological Survey Bulletin 2047. p. 313-317.

[41] A. J. Prata, "Infrared radiative transfer calculations for volcanic ash clouds", Geophysical Research Letters 16, 1293-1296 (1989).

[42] A. J. Prata and I. J. Barton, "Detection and discrimination of volcanic ash clouds by infrared radiometry - I: Theory", Proceedings of the First International Symposium on Volcanic Ash and Aviation Safety, U.S. Geological Survey Bulletin 2047, 305 - 311.

[43] I. J. Barton, A.J. Prata, I.G. Watterson, and S.A. Young, Identification of the Mount Hudson Volcanic Cloud over SE Australia", Geophysical Research Letters 19, 1211-1214 (1992).

[44] A. J. Prata and I. J. Barton, "Airborne Hazard Detection System - Project Overview", CSIRO Atmospheric Research, October 1999.

[45] Slater, David with CSIRO: Personal Communication by email. June 7, 2000.

[46] A. J. Prata, Private communication, October 4, 2000.

[47] D. Pieri, Private communication, July 28, 2000.

[48] Feasibility Study of Radiometry for Airborne Detection of Aviation Hazards - Subtask 2. Gary G. Gimmestad, Chris D. Papanicolopoulos, Mark A. Richards, Donald L. Sherman, and Leanne L. West. October, 2000.

[49] Mark Dombrowski, Vice President Spectral Optics Corporation. Email with document attachment "MIDIS Performance Specifications", Oct. 24, 2000.

[50] Mark Dombrowski, Vice President Spectral Optics Corporation. Personal Contact. Various dates in October, November, and December 2000.

[51] Stankov, B.B. and Bedard, A. J. Jr.: Remote Sensing of Winter Aircraft Icing Conditions. A Case Study, Journal of Aircraft, Vol. 31. No. 1, Jan.-Feb. 1994, p79-89.

[52] Keel, B. M.; Stancil, C. E.; Eckert; C. A.; Brown, S. M.; Gimmestad, G. G.; and Richards, M. A.: Aviation Weather Information Requirements Study. NASA/CR-2000-210288.

[53] Rauber, R. M. and Grant, L. O.: The Characteristics and Distribution of Cloud Water over the Mountains of North Colorado During Wintertime Storms. Part II: Spatial Distribution and Microphysical Characteristics. *Journal of Applied Meteorology*, Vol. 25, 1986, p. 489-504.

[54] Politovich, Marcia K.; Stankov, B. Boba; and Martiner, Brooks E.: Determination of Liquid Water Altitudes Using Combined Remote Sensors. 1995. Journal of Applied Meteorology, Vol. 34, pp. 2061-2075.1995.

[55] Vivekanandan; Martner, J. B.; and Politovich, M. K.: Aircraft Icing Detection Using Dual-Wavelength and Polarization Radar Observations. Presented at IEEE IGARSS'98.

[56] Reehorst, A.: NASA GRC, Cleveland, Ohio. Private communications. June 7, 2000.

[57] FAR Part 25 Appendix C continuous maximum envelope.

[58] Gavrilov, Nikolia and Taylor, Mike: What are Gravity Waves and Their Parameterization? PSMOS "Gravity Wave Parameterization" PROJECT. http://www.kurasc.kyoto-u.ac.jp/~psmosgw/gw_gen.htm#m1 Accessed June 23, 2000.

[59] Avery, Susan and Avery, James: University of Colorado Atmospheric Remote Sensing and Technology Group. Tropospheric Winds. Previous Research on Gravity Waves Over the Tropical Pacific. http://grison.colorado.edu/science/tropowinds.html Accessed June 23, 2000.

[60] Clear Air Turbulence (CAT). http://www-frd.fsl.noaa.gov/mab/scatcat/cat.html Accessed June 2, 2000.

[61] Schneider, David; Delene, David; Rose, William; and Wen, Shiming: Remote Sensing of Volcanic Eruption Clouds Using AVHRR. Two Channel AVHRR Discrimination of Volcanic Clouds. http://www.geo.mtu.edu/volcanoes/research/avhrr/discrim/ Accessed June 16, 2000.

[62] Hasegawa, Yohei: EUMETSAT. Volcanic Ash Cloud Tracking with GMS-5. September, 1996. http://www.eumetsat.de/en/area2/image/nov96/ref14.html Accessed June 16, 2000.

[63] Mosher, Frederick: Four Channel Volcanic Ash Detection Algorithm, October, 1999. http://www.awc-kc.noaa.gov/publications/mosher/paper3.html Accessed November 20, 1999.

| **REPORT DOCUMENTATION PAGE** | Form Approved<br>OMB No. 0704-0188 |
|---|---|



**1. AGENCY USE ONLY** (Leave blank)

**2. REPORT DATE**
June 2001

**3. REPORT TYPE AND DATES COVERED**
Contractor Report

**4. TITLE AND SUBTITLE**
Feasibility Study of Radiometry for Airborne Detection of Aviation Hazards

**5. FUNDING NUMBERS**
577-40-10-01

C NAS1-99073

**6. AUTHOR(S)**
Gary G. Gimmestad, Chris D. Papanicolopoulos, Mark A. Richards, Donald L. Sherman, and Leanne L. West

**7. PERFORMING ORGANIZATION NAME(S) AND ADDRESS(ES)**
Georgia Tech Research Institute
Georgia Institute of Technology
Atlanta, Georgia 30332-0800

**8. PERFORMING ORGANIZATION REPORT NUMBER**
GTRI-A6263

**9. SPONSORING/MONITORING AGENCY NAME(S) AND ADDRESS(ES)**
National Aeronautics and Space Administration
Langley Research Center
Hampton, VA 23681-2199

**10. SPONSORING/MONITORING AGENCY REPORT NUMBER**
NASA/CR-2001-210855

**11. SUPPLEMENTARY NOTES**
Langley Technical Monitor: James W. Johnson

**12a. DISTRIBUTION/AVAILABILITY STATEMENT**
Unclassified-Unlimited
Subject Category 33 Distribution: Standard
Availability: NASA CASI (301) 621-0390

**12b. DISTRIBUTION CODE**

**13. ABSTRACT** (Maximum 200 words)
Radiometric sensors for aviation hazards have the potential for widespread and inexpensive deployment on aircraft. This report contains discussions of three aviation hazards - icing, turbulence, and volcanic ash - as well as candidate radiometric detection techniques for each hazard. Dual-polarization microwave radiometry is the only viable radiometric technique for detection of icing conditions, but more research will be required to assess its usefulness to the aviation community. Passive infrared techniques are being developed for detection of turbulence and volcanic ash by researchers in this country and also in Australia. Further investigation of the infrared airborne radiometric hazard detection approaches will also be required in order to develop reliable detection/discrimination techniques. This report includes a description of a commercial hyperspectral imager for investigating the infrared detection techniques for turbulence and volcanic ash.

**14. SUBJECT TERMS**
Passive Microwave, Intraved, Remote Sensing, Aviation, Weather Hazards, Airborne, Airborne Detection

**15. NUMBER OF PAGES**
51

**16. PRICE CODE**

| 17. SECURITY CLASSIFICATION OF REPORT | 18. SECURITY CLASSIFICATION OF THIS PAGE | 19. SECURITY CLASSIFICATION OF ABSTRACT | 20. LIMITATION OF ABSTRACT |
|---|---|---|---|
| Unclassified | Unclassified | Unclassified | UL |